



Cite this: *Mater. Horiz.*, 2020, 7, 1971

Crystal regulation towards rechargeable magnesium battery cathode materials

Shuangshuang Tan,^a Fangyu Xiong,^a Junjun Wang,^a Qinyou An^{id}*^{ab} and Liqiang Mai^{id}*^{ab}

Rechargeable magnesium batteries (RMBs) as a promising energy storage system in terms of high abundance, greater electron transfer number and more uniform deposition behavior of the Mg metal anode have great potential for innovating the future energy storage markets. However, the large intercalation energy penalty and sluggish diffusion kinetics of bivalent Mg^{2+} in host materials due to the strong ionic polarization lead to unsatisfactory energy and power densities. Thus, constructing insertion sites and fast diffusion pathways for Mg^{2+} in cathode materials is significant for the development of RMBs. Herein, we systematically reviewed the recent developments of various crystal regulation strategies, including topochemical substitution, interlayer regulation, vacancy introduction, substitution doping, and amorphization, for improving the specific capacity, rate capability, redox potential and cycling stability of RMB cathode materials. The optimized mechanisms and regulation rules of various strategies for Mg^{2+} intercalation and diffusion were discussed in detail. The unique advantages of various strategies and the promising crystal systems were summarized. Moreover, the unexploited material systems, the untapped crystal regulation strategies, the current challenges and future objectives for high-energy and high-power RMBs are described.

Received 22nd February 2020,
Accepted 21st April 2020

DOI: 10.1039/d0mh00315h

rsc.li/materials-horizons

1. Introduction

Since 1991, lithium ion batteries (LIBs) have undergone tremendous development and dominated the market of portable electronic devices, and they are even going to revolutionize personal transportation with their use in electric vehicles.^{1–3} But the limited energy density on account of the inherent Li ion intercalation chemistry cannot satisfy the growing demand for a long driving range of electric vehicles (EVs).^{4,5} Therefore, Li metal anodes have been vigorously revived in recent years because of their high theoretical capacity (2061 mA h cm⁻³, 3860 mA h g⁻¹) and lowest redox potential (−3.04 V *versus* the standard hydrogen electrode (SHE)).^{6–9} Although the energy density of a Li metal pouch cell has been increased to 300 W h kg⁻¹, researchers are still finding it difficult to ensure its high safety and long life when used in the battery pack of electric vehicles.^{10,11} On the other hand, the dramatic depletion of scarce lithium resources drastically hinders the future applications of Li metal batteries in large-scale energy storage systems. Therefore, the present energy storage structure in the world is facing a significant challenge.^{12,13}

A low-cost and highly-safe energy storage system with high energy density needs to be urgently found.¹⁴

Rechargeable magnesium batteries (RMBs) as a promising alternative for LIBs have attracted wide interest and undergone explosive research development in the past decade owing to the large abundance of Mg (one of the most abundant elements, ~2% of Earth's crust), greater electron transfer number of Mg^{2+} and low reduction potential of Mg (−2.37 V *versus* SHE) (Fig. 1a).^{15,16} Compared to Li or Na metal anodes, the Mg metal anode possesses higher volumetric capacity (3833 mA h cm⁻³ for Mg vs. 2062 mA h cm⁻³ for Li and 1128 mA h cm⁻³ for Na).^{17,18} More importantly, the uniform deposition behavior of the Mg

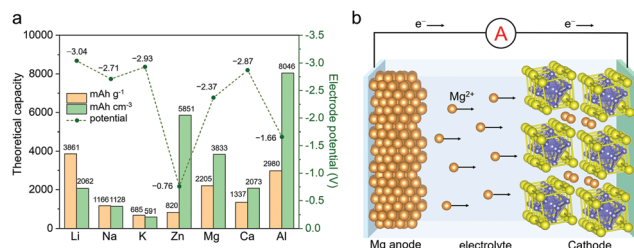


Fig. 1 (a) Theoretical capacities and redox potentials of various metal anodes. (b) Prototype of RMBs based on the Chevrel phase Mo_6S_8 cathode, magnesium halo-alkyl aluminate complex electrolyte and Mg metal anode.

^a State Key Laboratory of Advanced Technology for Materials Synthesis and Processing, Wuhan University of Technology, Wuhan 430070, China.
E-mail: mlq513@whut.edu.cn, anqinyou86@whut.edu.cn

^b Foshan Xianhu Laboratory of the Advanced Energy Science and Technology Guangdong Laboratory, Foshan 528200, Guangdong, China

metal anode in some electrolytes endows RMBs with higher safety.¹⁹ The key challenges of RMBs are developing anodically stable, high-efficiency Mg electrolytes²⁰ and high-performance Mg²⁺ host cathode materials.^{21,22} The first genuine breakthrough was the development of the organo-borate or organo-aluminate Mg electrolyte demonstrated by Gregory *et al.* in 1990.²³ Ten years later, Aurbach *et al.* presented a significant RMB prototype with a stable cycle life based on the insertable Chevrel phase Mo₆S₈ cathode, magnesium halo-alkyl aluminate complex electrolyte and Mg metal anode (Fig. 1b).²⁴ Unfortunately, its limited specific capacity and relatively low voltage provided it with little potential to replace LIBs in that period. Subsequently, developing high-capacity, high-voltage, high-rate and long-life cathode materials became the subject of ongoing research in the RMB field.

The source of challenges in RMB cathode materials is the inherently strong ionic polarization force of bivalent Mg²⁺ owing to the high charge/radius ratio, which leads to strong electrostatic interactions between Mg²⁺ and host anion lattices.^{18,25} Thus, most inorganic materials showed sluggish Mg²⁺ diffusion kinetics, further resulting in serious voltage polarization/hysteresis and a low magnesianation degree.²⁶ Moreover, some classical materials in LIBs cannot effectively deliver Mg²⁺ intercalation capacity due to the limited Mg²⁺ storage sites and winding migration path.²⁷ In order to obtain acceptable Mg²⁺ storage, diffusion kinetics and formation energies in host materials, crystal regulation is indispensable to create Mg²⁺ storage sites, expand Mg²⁺ migration channels, shield the strong polarization of Mg²⁺, reduce the interaction from the host, and even increase the redox potential. Thus, summarizing the recent developments and regulation rules of various strategies is significant to promote the development of RMB cathodes. However, so far, the related reviews have not been reported.

In this review, we will summarize the various crystal regulation strategies for high-performance RMB cathode materials, including topochemical substitution, substitution doping, interlayer regulation, vacancy introduction and amorphization (Fig. 2). The optimized mechanisms and regulation rules of various strategies for Mg²⁺ diffusion and storage will be systematically discussed, in which the representative and promising cathode materials are also highlighted. The fundamental works and experimental results will be naturally integrated for review. Some controversial viewpoints are going to be proposed and discussed. Moreover, the promising Mg storage materials, systems and modification strategies for future high-energy and high-power RMBs are described. We hope that this review can provide some inspiration as the “key” to unlock the “crystal house” for fast and stable Mg²⁺ migration and storage.

2. Topochemical substitution in the main crystal structures for RMBs

In an attempt to obtain the available crystal frameworks for reversible divalent Mg²⁺ intercalation/de-intercalation, replacing the A-site ions with Mg²⁺ in some insertable materials (*i.e.*, topochemical substitution) is an effective method.²⁸ This method can maintain the original framework relatively well and allows Mg²⁺ to reversibly

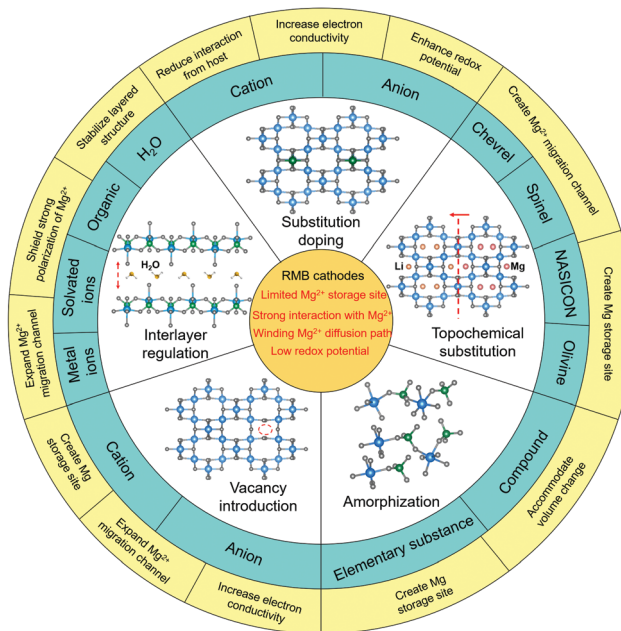


Fig. 2 Overview of various crystal regulation strategies for high-performance RMB cathode materials.

diffuse in the framework and occupy the electrochemically active A site.²⁹ Up to now, the main insertion-type materials, including Chevrel, spinel, NASICON, olivine phase and so forth, have been obtained by topochemical substitution, and they have exhibited unique electrochemical performances in RMBs. In this section, we will review the research progress and challenges of the main insertion-type RMB cathode materials, while highlighting the advantages of topochemical substitution for preparing these materials.

2.1. Chevrel phase

The Chevrel phase was first reported by Chevrel *et al.* in 1971; the general formula can be expressed as A_xⁿ⁺Mo₆X₈, where A = metal, and X = S or Se.³⁰ It was found to be a favorable framework for the fast migration of monovalent,³¹ divalent,^{24,32,33} and even trivalent cations.³⁴ The Chevrel framework is different from the structures of commercialized LIB cathode materials with close-packed oxygen anion sublattices; it is composed of Mo₆X₈ blocks, where 8 X anions as the vertex form an X₈ cube and 6 Mo on the cube faces constitute a Mo₆ octahedron (Fig. 3a). The arrangement of Mo₆X₈ blocks results in three different cavities (cavity 1, cavity 2 and cavity 3). Cavity 1, cavity 2 and cavity 3 share corners, edges and faces with the Mo₆X₈ cubes, respectively. The intercalating A-site ions are usually located in cavity 1 and cavity 2, because cavity 3 is the closest to the Mo atoms, which leads to strong electrostatic repulsion between intercalating ions and Mo atoms.^{17,35} In cavity 1, a ring of six “inner sites” could be occupied by the small ions, such as Li⁺, Na⁺, Mg²⁺ and so forth. Meanwhile, six “outer sites” in cavity 2 around cavity 1 are also able to be occupied (inset of Fig. 3b). Although the Chevrel phase has available ionic conductivity for many cations owing to the up to 12 possible sites and acceptable hopping energy barriers between sites, it is difficult to synthesize Mg_xMo₆X₈ directly by chemical

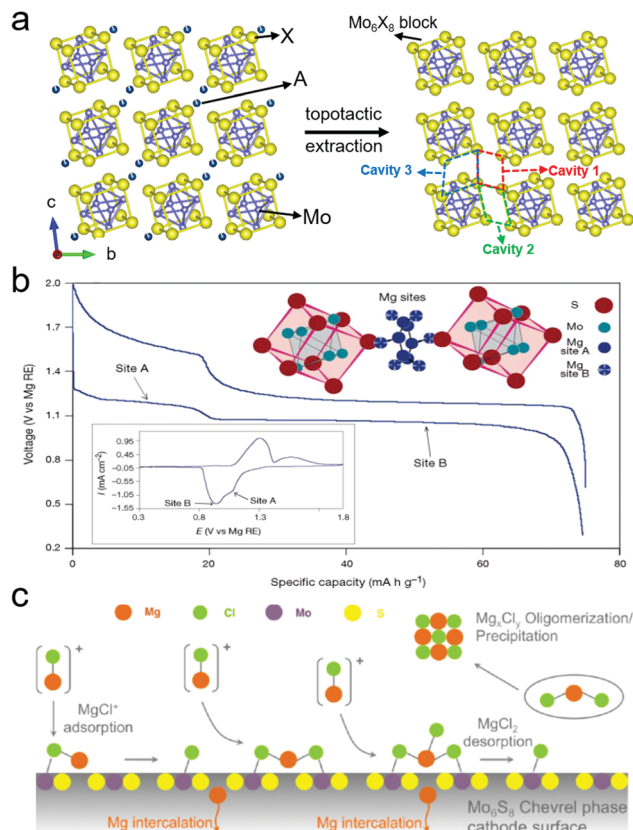


Fig. 3 (a) Crystal structure of $A_x\text{Mo}_6\text{X}_8$ and Mo_6X_8 . A = metal and X = S or Se. (b) Galvanostatic charge–discharge curve and CV curve of $\text{Mg}_x\text{Mo}_6\text{S}_8$ in $\text{Mg}(\text{AlCl}_2\text{BuEt})_2/\text{THF}$ electrolyte and distribution of Mg^{2+} in the fully discharged Mo_6S_8 structure (reproduced from ref. 24, with permission from Nature Publishing Group). (c) Schematic of Mg desolvation, adsorption and intercalation on the Mo_6S_8 surface in a halide electrolyte (reproduced from ref. 36, with permission from the American Chemical Society).

methods, and thus the topochemical substitution strategy has important significance for Mg^{2+} intercalation in the Chevrel phase.

In 2000, Aurbach *et al.* prepared Chevrel phase Mo_6S_8 by topochemical extraction reaction.²⁴ $\text{Cu}_2\text{Mo}_6\text{S}_8$ was firstly synthesized by high-temperature solid-state reaction and then Cu atoms were extracted from $\text{Cu}_2\text{Mo}_6\text{S}_8$ by chemical etching using an aqueous FeCl_3 solution. Finally, Mg ions could be inserted electrochemically into Mo_6S_8 in the $\text{Mg}(\text{AlCl}_2\text{BuEt})_2/\text{tetrahydrofuran}$ (butyl: Bu; ethyl: Et; THF) electrolyte, and they tended to insert into site A (cavity 1) and then site B (cavity 2), resulting in two straight potential platforms at 1.2 and 1.0 V (Fig. 3b). Moreover, Mo atoms on the Mo_6S_8 surface could facilitate the breaking of the Mg–Cl bond, leading to the reversible intercalation of Mg ions (Fig. 3c).³⁶ Favorable compatibility between Mo_6S_8 or other Mo-based materials and halide electrolytes was also suggested. But the following passivation of Cl^- and precipitation of Mg_xCl_y species may result in a higher barrier of Mg^{2+} intercalation. The obtained Mo_6S_8 usually displayed a discharge capacity of $\sim 100 \text{ mA h g}^{-1}$ at room temperature, which was lower than the theoretical capacity of $128.8 \text{ mA h g}^{-1}$, mainly owing to the relatively slow kinetics of Mg^{2+} intercalation in site A and large hopping

energy barriers from site A to B.^{35,37,38} The experimental average diffusion coefficient of Mg^{2+} (D_{Mg}) in Mo_6S_8 could reach $2.6 \times 10^{-12} \text{ cm}^2 \text{ s}^{-1}$ based on the potentiostatic intermittent titration (PITT) result.³⁹ Although it exhibited acceptable Mg^{2+} mobility kinetics and excellent cycling stability, the low working voltage and specific capacity resulted in a low energy density, which still limited its practical applications. Therefore, the exploration of high-voltage cathode materials is of great significance to the development of RMBs. Next, we will review some promising cathode materials with higher voltages and reversible capacity for RMBs, which are prepared by topochemical substitution, such as spinel, NASICON, olivines, *etc.*

2.2. Spinel phase

Spinel materials (space group $Fd\bar{3}m$) are a family of materials with the general formula AT_2X_4 , where X can be a chalcogen; A is usually a bivalent metal element, such as Mg, Cu, Zn and so forth; and T is a trivalent metal element (Ti, Mn, Co, Ni, Cr and so forth). A and T are tetrahedrally and octahedrally coordinated by X, respectively, and the $[\text{TX}_6]$ octahedra are interconnected by edge-sharing, forming the three-dimensional diffusion channels (Fig. 4a). Thackeray *et al.* first prepared the spinel LiMn_2O_4 as a cathode material for LIBs.⁴⁰ It usually exhibited a high operating potential around 3–4 V and specific capacity over 200 mA h g^{-1} .^{41,42} In addition, the electrochemical properties (potential, specific capacity, cycling life, *etc.*) of spinel

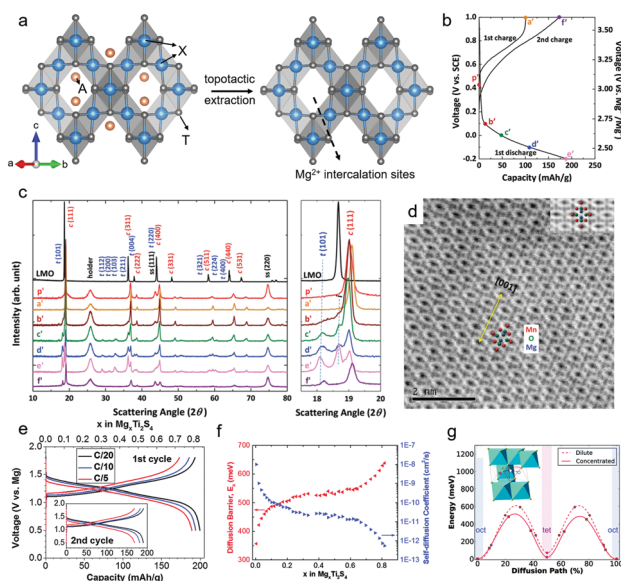


Fig. 4 (a) Crystal structure of spinel AT_2X_4 and T_2X_4 obtained by topochemical extraction of A. The A atoms and T atoms are located at tetrahedral and octahedral sites, respectively. T = Mn, Fe, Co, V, Cr, Ti, Ni and so forth; X = O, S or Se. (b) Charge and discharge curves of the acid-treated LiMn_2O_4 electrode in $1 \text{ M Mg}(\text{NO}_3)_2/\text{H}_2\text{O}$. (c) *Ex situ* XRD patterns of LiMn_2O_4 in different discharge/charge states. (d) ABF STEM image of $\text{Mg}_x\text{Mn}_2\text{O}_4$ at -0.2 V vs. SCE . Reproduced from ref. 50, with permission from Wiley-VCH. (e) Charge and discharge curves of the Ti_2S_4 electrode at various rates in APC/THF electrolyte at 60°C . Mg^{2+} self-diffusion coefficients and the corresponding energy barriers in Ti_2S_4 determined by GITT at 60°C (f) and DFT calculation (g) (reproduced from ref. 58, with permission from the Royal Society of Chemistry).

compounds could be adjusted by changing or doping the T element.^{43,44} Therefore, spinel compounds show promising prospects for application in LIBs, sodium ion batteries (SIBs) and even multivalent ion batteries. The DFT calculations showed Mg^{2+} diffusion energy barriers of 650–850 meV between the tetrahedral sites in Mn_2O_4 , Co_2O_4 , Cr_2O_4 and Ni_2O_4 ,⁴³ which suggested the feasibility of Mg^{2+} storage in spinel oxides. Okamoto *et al.* synthesized a series of magnesium spinel oxides for investigating the Mg intercalation and push-out mechanisms, including MgCo_2O_4 , MgMn_2O_4 , MgFe_2O_4 , and MgCr_2O_4 , by high-temperature solid phase reaction.⁴⁵ Unfortunately, reversible Mg insertion and extraction were only observed at high-temperature during electrochemical testing (about 150 °C). Meanwhile, the cation disorder phenomenon that the A-site atom occupies the octahedral sites (rocksalt structure) rather than the typical tetrahedral sites may occur in spinel compounds in the case of a high A concentration during the high-temperature solid phase reaction.^{43,46} In MgMn_2O_4 , the presence of the rocksalt structure will inhibit the Mg^{2+} intercalation reaction, leading to the loss of half the theoretical capacity.⁴⁷ To avoid the formation of the rocksalt structure, electrochemical or chemical topotactic substitution as a mild method may be more effective to obtain spinel MgMn_2O_4 .

Sinha *et al.* prepared the well-ordered MgMn_2O_4 by an electrochemical conversion process involving delithiation of cubic spinel LiMn_2O_4 in 5 M $\text{LiNO}_3/\text{H}_2\text{O}$ and the following magnesianation in 1 M $\text{Mg}(\text{NO}_3)_2/\text{H}_2\text{O}$.⁴⁸ The obtained MgMn_2O_4 presented reversible Mg^{2+} insertion/extraction with a discharge capacity of $\sim 41 \text{ mA h g}^{-1}$. X-ray Diffraction (XRD) result revealed that the obtained MgMn_2O_4 was converted to a tetragonal structure, owing to the lattice distortion after the reduction of Mn^{4+} to Mn^{3+} upon Mg^{2+} insertion. A similar work was reported by Yuan *et al.*,⁴⁹ in which a high specific capacity of $478.4 \text{ mA h g}^{-1}$ at 13.6 mA g^{-1} in 1 M MgCl_2 aqueous electrolyte could be obtained. In addition, Cabana *et al.* deeply illuminated the phase transformation from LiMn_2O_4 to MgMn_2O_4 by using *ex situ* XRD, atom-level scanning transmission electron microscopy (STEM) and X-ray absorption spectroscopy (XAS) measurements.⁵⁰ The spinel $\lambda\text{-Mn}_2\text{O}_4$ could be firstly prepared by acid treatment and electrochemical charging of $\text{Li}_2\text{Mn}_2\text{O}_4$, and then Mg could be inserted into $\lambda\text{-Mn}_2\text{O}_4$ in 1 M $\text{Mg}(\text{NO}_3)_2/\text{H}_2\text{O}$ (Fig. 4b). It delivered a high discharge capacity of $\sim 190 \text{ mA h g}^{-1}$ with an average working voltage of $\sim 2.5 \text{ V vs. Mg}^{2+}/\text{Mg}$. During the discharge process, the structure distortion from cubic (spinel) to tetragonal phases resulting from the Jahn–Teller distortion due to increasing amounts of Mn^{3+} was confirmed (Fig. 4c), which is consistent with the observation by Sinha *et al.* Meanwhile, an intermediate between the cubic and tetragonal phases could be detected. Nevertheless, the Mg-inserted $\lambda\text{-Mn}_2\text{O}_4$ still kept the major spinel phase, which was further demonstrated by the ABF STEM image of $\lambda\text{-Mn}_2\text{O}_4$ at $-0.2 \text{ V vs. saturated calomel electrode (SCE)}$ (Fig. 4d). These results indicated that topochemical substitution is able to relatively maintain the cubic spinel structure of MgMn_2O_4 and further control the delithiation and magnesianation. To date, other spinel metal oxides have

not been prepared by topochemical substitution for the RMB cathodes.^{51–55}

In order to achieve higher Mg^{2+} diffusion kinetics in the host, some thiospinels were subsequently explored as cathode materials for RMBs.^{56,57} As the radius of S atoms is larger than that of O atoms, thiospinels possess a larger ion diffusion channel and show a decreasing interaction with Mg ions. DFT calculations showed that the diffusion energy barriers of Mg^{2+} in Mn_2S_4 , Cr_2S_4 and Ti_2S_4 are 515 meV, 567 meV and 615 meV, respectively,⁵⁶ which are distinctly lower than those of the corresponding spinel metal oxides. Nazar and co-workers reported the Ti_2S_4 thiospinel as a cathode material for RMBs prepared from CuTi_2S_4 by chemical Cu^+ extraction.⁵⁸ The obtained Ti_2S_4 delivered an initial discharge capacity of $\sim 200 \text{ mA h g}^{-1}$ ($\sim 0.8 \text{ Mg per formula}$) with an average working voltage of 1.2 V in an all phenyl complex/tetrahydrofuran (APC/THF) electrolyte at 60 °C (Fig. 4e). Upon Mg intercalation/deintercalation, the cubic spinel phase was reversibly preserved, while a moderate volume expansion of 10% promoted good capacity retention. In the Ti_2S_4 lattice, D_{Mg} and the corresponding energy barrier of Mg^{2+} were calculated as $5 \times 10^{-10} \text{ cm}^2 \text{ s}^{-1}$ and 550 meV based on the galvanostatic intermittent titration technique (GITT) result, respectively (Fig. 4f). This result agrees very well with the DFT calculated value (Fig. 4g). In addition, Nazar's group revealed the Mg^{2+} occupation situation in spinel Ti_2S_4 compared to monovalent Li^+ .⁵⁹ They found that the D_{Mg} in spinel Ti_2S_4 was equal to that of Li^+ (D_{Li}) in the initial discharge state, which implied that ionic charge did not play a large role in the Ti_2S_4 lattice. However, when the insertion amount of Mg^{2+} (x) was greater than 0.55, D_{Mg} decreased by $\sim 10\text{--}20$ times compared to D_{Li} . This was due to the fact that the tetrahedral site occupation of Mg^{2+} blocks the diffusion pathway between the four nearest-neighbor octahedral sites (octahedral–tetrahedral–octahedral). In contrast, the inserted Li^+ only occupies the octahedral site of spinel Ti_2S_4 for any composition.⁶⁰ This result explains why $\text{Mg}_x\text{Ti}_2\text{S}_4$ could not be discharged beyond $x = 0.8$. The above-mentioned works demonstrate that magnesium spinel and thiospinel compounds can be obtained by topochemical substitution and exhibit reversible Mg^{2+} insertion/extraction. But most DFT-predicted spinel materials still lack experimental synthesis and investigation, such as Mn_2S_4 , Cr_2S_4 and so forth, although the corresponding AT_2X_4 has been reported.^{61,62} In addition, how to accurately control the degree of A-site ion substitution to avoid some inactive phase in spinel compounds is significant and remains difficult. Thorough investigations on Mg^{2+} intercalation/extraction mechanisms and lots of experiments are indispensable.

2.3. NASICON structures

Sodium super ionic conductors (NASICON) with the general formula $\text{A}_x\text{M}_2(\text{XO}_4)_3$ ($\text{A} = \text{Li, Na, K, Ca, Mg}$; $\text{M} = \text{Ti, V, Fe, Zr, Mn}$; and $\text{X} = \text{S, P, Si, As}$) and various crystal structures (rhombohedral, monoclinic, triclinic, orthorhombic and so forth) have been extensively studied in LIBs and SIBs owing to their high ionic conductivity and excellent structural stability.^{63,64}

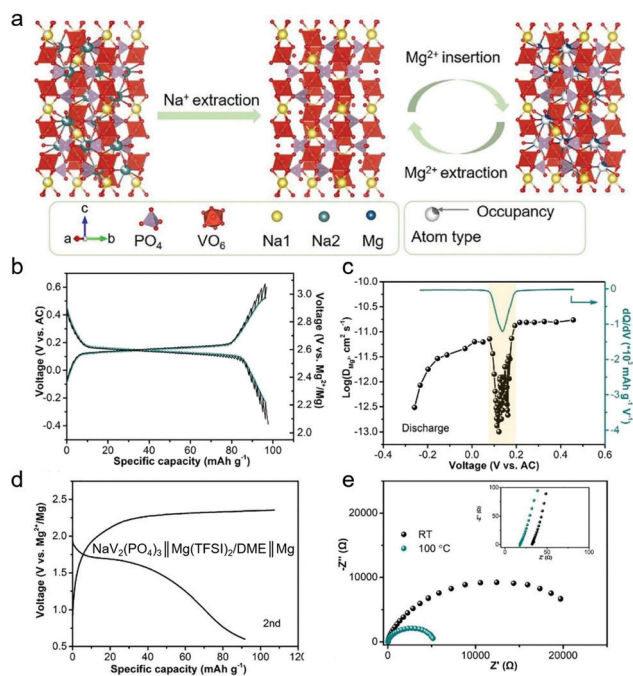


Fig. 5 (a) Topochemical substitution of Mg^{2+} in NASICON $\text{Na}_3\text{V}_2(\text{PO}_4)_3$ phase. (b) The GITT curves of $\text{NaV}_2(\text{PO}_4)_3/\text{C}$ in $\text{Mg}(\text{TFSI})_2/\text{AN}$ electrolyte. (c) D_{Mg} for the $\text{NaV}_2(\text{PO}_4)_3/\text{C}$ electrode during the discharge process. (d) Charge/discharge curves of the full cell ($\text{NaV}_2(\text{PO}_4)_3/\text{C}||\text{Mg}(\text{TFSI})_2/\text{DME}||\text{Mg}$) at the second cycle (0.05C, 100 °C). (e) Nyquist plots of the Mg full cell at room temperature and 100 °C at open-circuit voltage. Reproduced from ref. 70, with permission from Elsevier.

The NASICON structure formed by corner-shared $[\text{MO}_6]$ octahedra and $[\text{XO}_4]$ tetrahedra has a large interstitial space that can hold up to 5 alkali metal ions per formula (Fig. 5a). Importantly, the large interstitial space suggests that the NASICON structure has large potential to become a Mg^{2+} host for reversible insertion/extraction. Moreover, the high ionic conductivity and excellent structural stability may facilitate a fast and stable diffusion of Mg^{2+} in the NASICON structure. To date, some thermodynamically stable $\text{Mg}_x\text{M}_2(\text{XO}_4)_3$ materials, such as $\text{Mg}_{0.5}\text{Ti}_2(\text{PO}_4)_3$,⁶⁵ $\text{Mg}_{0.5+y}(\text{Fe}_y\text{Ti}_{1-y})_2(\text{PO}_4)_3$,⁶⁶ and $\text{Mg}_{0.5}\text{Zr}_2(\text{PO}_4)_3$,⁶⁷ have been prepared by sol-gel and annealing methods. These NASICON materials all exhibited the ability for electrochemical Mg^{2+} diffusion but a slow diffusion kinetics of Mg^{2+} , and the researchers did not reveal the reversible Mg^{2+} extraction behavior. Other thermodynamically stable, even metastable $\text{Mg}_x\text{M}_2(\text{XO}_4)_3$ materials with possibly higher potentials or specific capacities were not synthesized. Topochemical substitution is more effective to maintain the crystal framework and enable Mg^{2+} to occupy the A site, and thus it is appropriate for the preparation of some thermodynamically stable, even metastable $\text{Mg}_x\text{M}_2(\text{XO}_4)_3$ materials.

Huang *et al.* obtained the $\text{V}_2(\text{PO}_4)_3/\text{C}$ materials by electrochemical delithiation of monoclinic $\text{Li}_3\text{V}_2(\text{PO}_4)_3/\text{C}$ in LIBs at 55 °C.⁶⁸ The charge capacity of 197 mA h g^{-1} corresponds to three extracted Li^+ ions from $\text{Li}_3\text{V}_2(\text{PO}_4)_3/\text{C}$. The obtained $\text{V}_2(\text{PO}_4)_3/\text{C}$ delivered a reversible capacity of 197 mA h g^{-1} at C/20 with an average working voltage of 2.7 V vs. Mg^{2+}/Mg

at 55 °C. Unfortunately, $\text{V}_2(\text{PO}_4)_3/\text{C}$ exhibits poor cycling stability (<10 cycles), which may result from the large structural distortion of $\text{V}_2(\text{PO}_4)_3/\text{C}$ during the reversible Mg^{2+} (de)intercalation. Zeng *et al.* reported a more stable $\text{NaV}_2(\text{PO}_4)_3$ framework prepared by electrochemical desodiation from rhombohedral $\text{Na}_3\text{V}_2(\text{PO}_4)_3/\text{C}$ at the expense of a lower capacity (Fig. 5a).^{69,70} It exhibited a discharge capacity of $\sim 96 \text{ mA h g}^{-1}$ ($\sim 0.75 \text{ Mg}$) with an average working voltage of $\sim 2.5 \text{ V vs. Mg}^{2+}/\text{Mg}$ during the GITT test (Fig. 5b). *Ex situ* XRD indicated that the Mg^{2+} storage mechanism of $\text{NaV}_2(\text{PO}_4)_3/\text{C}$ is a two-phase transition reaction, which is similar to the Na^+ insertion behavior in $\text{NaV}_2(\text{PO}_4)_3$. But an ambiguous point is whether the residual Na in $\text{NaV}_2(\text{PO}_4)_3/\text{C}$ is replaced by the inserted Mg^{2+} during the following cycles. The replacement mechanism from inherent Li^+ to the intercalated Mg^{2+} in spinel $\text{Li}_4\text{Ti}_5\text{O}_{12}$ was observed.⁷¹ Upon the intercalation of 0.75 Mg in $\text{NaV}_2(\text{PO}_4)_3/\text{C}$, the D_{Mg} ranged from 1.90×10^{-11} to $1.02 \times 10^{-13} \text{ cm}^2 \text{ s}^{-1}$ (Fig. 5c), which is close to the D_{Mg} in Chevrel and spinel phases. In addition, the Mg full cell assembled with the $\text{NaV}_2(\text{PO}_4)_3/\text{C}$ cathode, magnesium bis(trifluoromethylsulfonyl)imide/dimethoxyethane ($\text{Mg}(\text{TFSI})_2/\text{DME}$) and Mg anode exhibited a discharge capacity of 92 mA h g^{-1} at the second cycle but a low average discharge voltage of 1.3 V at 100 °C (Fig. 5d). Although the high temperature decreased the interfacial transfer impedance of Mg^{2+} on the cathode (Fig. 5e), it aggravated the decomposition of DME at high potential, leading to the absence of redox at 2.5 V vs. Mg^{2+}/Mg . Therefore, choosing Mg electrolytes with high oxidation stability and good compatibility is critical for the application of high-voltage RMB cathodes. In addition, various M-site atoms, such as Co, Fe, Mn, Cr, and so forth, could be selected to obtain a higher voltage or capacity.

In addition to the electrochemical extraction of Li/Na, the chemical reaction between the oxidizing agents, I_2 ,⁷² NOBF_4 or NO_2BF_4 , and $\text{Na}_3\text{M}_2(\text{PO}_4)_3$ could also be used to prepare $\text{NaM}_2(\text{PO}_4)_3$ materials. This avoids electrode handling and the mixing of binder and carbon black. But how to stabilize the delithiated or desodiated metastable phase in the chemical process still requires attention.

2.4. Olivine phase

Since olivine LiFePO_4 has been widely studied and used in commercial LIBs, olivine MgMXO_4 ($\text{M} = \text{Fe, Mn, Co, Ni, etc.}$; $\text{X} = \text{P, Si}$) have attracted plenty of attention as RMB cathode materials, owing to their high theoretical capacity and potential (such as MgFeSiO_4 : theoretical capacity of $\sim 362.4 \text{ mA h g}^{-1}$ and theoretical working voltage of $\sim 2.4 \text{ V vs. Mg}^{2+}/\text{Mg}$).^{73–81} In orthorhombic olivine MgMXO_4 ($Pnmb$ space group), transition metal atoms usually occupy 4c sites (M2 site) and form linear chains of edge-sharing MO_6 octahedra along the bc plane, and XO_4 tetrahedra share corners and edges with the MO_6 octahedra (Fig. 6a). Mg ions usually occupy 4a sites (M1 site) in the one-dimensional (1D) channels along the c -axis.^{82,83} In the olivine MgMXO_4 structure, two challenges have been substantially discussed since 2000. The first is how to control the degree of anti-site mixing of Mg and M ions. A clear consensus is that the degree of mixing is temperature-dependent.

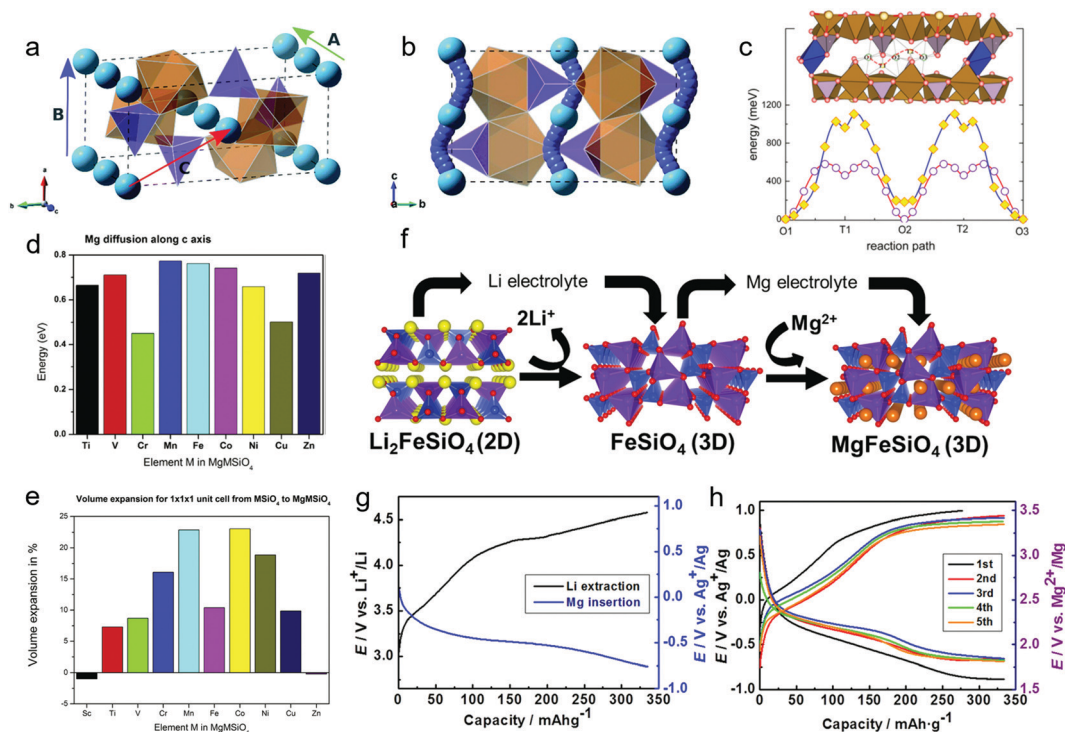


Fig. 6 (a) The crystal structure of olivine MgMXO₄ and the Mg-ion migration pathways (brown octahedra: MO₆, purple tetrahedra: XO₄, blue spheres: Mg ions). (b) The curved Mg²⁺ pathway parallel to the *c*-axis with the lowest energy. Reproduced from ref. 82, with permission from the Royal Society of Chemistry. (c) Mg²⁺ diffusion energy barriers in the wave-like octahedral–tetrahedral–octahedral path of olivine FePO₄ (open circle) and Mg_{0.5}FePO₄ (solid diamond) (red: O; brown: Fe; purple: P; blue: Mg) (reproduced from ref. 85, with permission from the American Chemical Society). Statistics of energy barriers for Mg diffusion in various MgMSiO₄ (d) and unit cell expansion from MSiO₄ to MgMSiO₄ (e) (reproduced from ref. 86, with permission from Elsevier). (f) Synthesis and (g) charge–discharge profiles of metastable orthorhombic MgFeSiO₄ from Li₂FeSiO₄ by topochemical substitution. (h) Charge–discharge curves of metastable MgFeSiO₄ with a current density of 6.62 mA g⁻¹ in 0.5 M Mg(TFSI)₂/AN electrolyte at 55 °C. Reproduced from ref. 87, with permission from Nature Publishing Group.

In MgFeSiO₄, Redfern *et al.* thought that Mg ions tend to occupy the M1 site with the increase of synthesis temperature, especially over 900 °C, as demonstrated by *in situ* neutron powder diffraction.⁷³ However, Nuli and co-workers and Uchimoto's group thought that high temperature would lead to the increase of Mg occupation at the M2 site (M at the M1 site) in MgFeSiO₄ and MgMnSiO₄ according to electrochemical measurements and XRD analysis, respectively.^{78,84} When the M ions occupy the M1 site, the Mg diffusion channel may be blocked and the number of Mg storage sites might decrease, which would result in low specific capacity and severe polarization.^{82,83} Therefore, revealing the real relationship between temperature and anti-site defect degree, and further eliminating the anti-site defects are important for optimizing the electrochemical performance of olivine MgMXO₄ materials.

Another challenge is how to improve the Mg²⁺ diffusion kinetics in the olivine framework. DFT calculations indicated that the migration energy barrier of Mg²⁺ along the *c* axis (path A) is the lowest (Fig. 6a). The “waviness” migration pathway is similar to the diffusion of Li⁺ in olivine LiFePO₄ (Fig. 6b), but the theoretical D_{Mg} (10⁻²⁰ cm² s⁻¹, 1025 meV) is twelve orders of magnitude below D_{Li} (10⁻⁸ cm² s⁻¹, 270 meV) along the octahedral–tetrahedral–octahedral path (Fig. 6c).⁸⁵ The reduced diffusivity was due to the large intercalation energy penalty of Mg²⁺

into the intermediate tetrahedral site. The occupation of Mg at the tetrahedral site may induce a trajectory for Mg²⁺ migration toward direct octahedral–octahedral hopping, leading to a larger activation energy barrier. The delithiated FePO₄ just displayed a low specific capacity of ~13 mA h g⁻¹ at 20 μA cm⁻² without any clear voltage plateau. This was also due to the formation of an inactive amorphous surface layer on the FePO₄ bulk that impedes Mg²⁺ intercalation from the surface into the bulk.

Compared with the olivine phosphates, silicates exhibit a more stable and faster framework for Mg²⁺ storage and migration owing to the fact that the compact SiO₄ tetrahedra can afford intrinsic lattice stabilization.⁷⁸ Meanwhile, the strong inductive effect of SiO₄ can weaken the redox couple of M to generate a relatively high potential. Chen *et al.* investigated the Mg²⁺ diffusion energy barrier along the *c* axis in various olivine silicates, such as MgCrSiO₄, MgFeSiO₄, MgNiSiO₄ and so forth, by DFT calculations (Fig. 6d).⁸⁶ The average energy barrier is ~600 meV, which is lower than that of FePO₄. MgCrSiO₄ exhibits the lowest Mg diffusion energy barrier of ~450 meV. Moreover, the volume expansion ratio of various MgTMSiO₄ compounds was also summarized, when all Mg was removed (Fig. 6e). The smallest expansion was observed for Ti, V and Fe.

In an attempt to avoid the anti-site defects in high-temperature solid phase reaction and improve the Mg diffusion

in MgTMSiO_4 , Orikasa *et al.* synthesized a metastable orthorhombic MgFeSiO_4 by topochemical substitution (Fig. 6f).⁸⁷ Firstly, two Li^+ ions were removed from the monoclinic $\text{Li}_2\text{FeSiO}_4$ structure with a two-dimensional (2D) network of SiO_4 and FeO_4 tetrahedra in LIBs, and then Mg^{2+} ions were inserted into the delithiated three-dimensional (3D) orthorhombic FeSiO_4 in $\text{Mg}(\text{TFSI})_2/\text{acetonitrile}$ (AN) (Fig. 6g), which can achieve an orderly occupancy of Mg and Fe in MgFeSiO_4 . Meanwhile, the tetrahedrally coordinated Mg could facilitate Mg^{2+} diffusion more than octahedrally coordinated Mg. Therefore, the metastable MgFeSiO_4 exhibited a high electrochemical activity and reversible Mg ion (de)insertion with a discharge capacity of 330 mA h g^{-1} and a high voltage of $\sim 2.4 \text{ V}$ vs. Mg^{2+}/Mg at 55°C (Fig. 6h). The estimated energy density of $\sim 746 \text{ W h kg}^{-1}$ dramatically exceeds that of Mo_6S_8 (135 W h kg^{-1}). On the other hand, replacing the SiO_4 tetrahedra by Si_3O_4 tetrahedra to reduce the interaction between Mg^{2+} and the host framework can also improve Mg^{2+} diffusion.⁸⁸ But the related MgMSi_4 materials have not been synthesized.

2.5. Metastable V_2O_5

In addition to the main Chevrel, spinel, NASICON and olivine materials, some DFT-predicted metastable materials or analogues of LIB cathode materials have also been given much attention. For example, V_2O_5 has many polymorphs, such as $\alpha\text{-V}_2\text{O}_5$, metastable $\zeta\text{-V}_2\text{O}_5$, bilayer $\varepsilon\text{-V}_2\text{O}_5$ and so forth.^{89–91} The possible Mg^{2+} migration channels and the corresponding energy barriers were systematically calculated. Among these materials, the migration barriers of Mg^{2+} in metastable $\zeta\text{-V}_2\text{O}_5$ and metastable $\varepsilon\text{-V}_2\text{O}_5$ were approximately 0.62–0.86 and 0.21–0.24 eV, respectively, which give them significant potential as RMB cathodes. Metastable $\zeta\text{-V}_2\text{O}_5$ and $\varepsilon\text{-V}_2\text{O}_5$ usually need to be synthesized under high temperature and pressure conditions, and thus are rarely reported in RMBs. Andrews *et al.* successfully prepared the metastable $\zeta\text{-V}_2\text{O}_5$ by topochemical extraction of the Ag ion of $\zeta\text{-Ag}_{0.33}\text{V}_2\text{O}_5$ in hydrochloric acid (Fig. 7a).⁹² The metastable $\varepsilon\text{-V}_2\text{O}_5$ may be obtained by similar topochemical extraction from $\varepsilon\text{-Cu}_x\text{V}_2\text{O}_5$.⁹³ The metastable $\zeta\text{-V}_2\text{O}_5$ is composed of distorted VO_6 octahedra and VO_5 square pyramids, where the edge-sharing and corner-sharing VO_6 octahedral layers are linked by VO_5 square pyramids. The 1D channel along the *b* axis with two distinct sites for ion intercalation is enclosed by these polyhedra. Then, Mg^{2+} could be inserted into the metastable $\zeta\text{-V}_2\text{O}_5$ by chemical or electrochemical methods. After 100 cycles, the metastable $\zeta\text{-V}_2\text{O}_5$ displayed a specific capacity of approximately 100 mA h g^{-1} with 1.0 V vs. Mg^{2+}/Mg in $\text{Mg}(\text{TFSI})_2/\text{AN}$ electrolyte (Fig. 7b), which indicates that the tunnel structure is beneficial for Mg^{2+} reversible (de)intercalation. However, the unsatisfactory coulombic efficiency suggests limited intercalation kinetics, especially during demagnesian (Fig. 7c).

2.6. Fluorinated polyanionic salts

Fluorinated polyanionic salts have been largely employed in LIBs due to their high working voltage, high capacity and fast Li^+ diffusivity.⁹⁴ In light of this, Wu *et al.* proposed the triclinic MgVPO_4F as a RMB cathode material using first principles calculations.⁹⁵

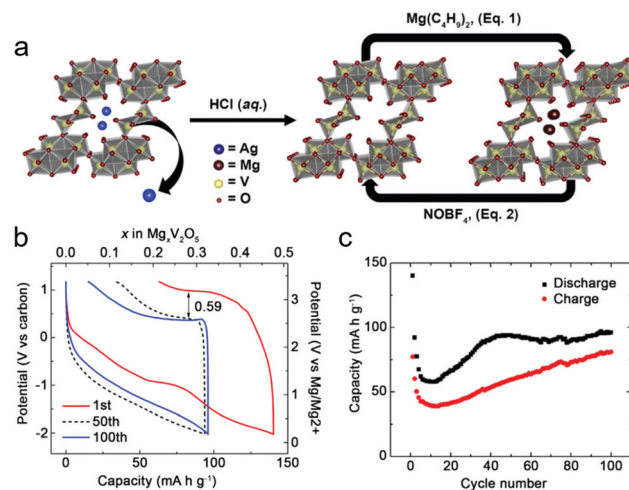


Fig. 7 (a) Schematic illustration of the synthesis processes of the metastable $\zeta\text{-V}_2\text{O}_5$. (b) Charge–discharge curves of the metastable $\zeta\text{-V}_2\text{O}_5$ at the 1st, 50th, and 100th cycles. (c) Cycling performance of the metastable $\zeta\text{-V}_2\text{O}_5$. Reproduced from ref. 92, with permission from Cell Press.

As shown in Fig. 8a, MgVPO_4F consists of corner-shared VO_4F_2 octahedral layers connected by PO_4 tetrahedra, with Mg^{2+} occupying the framework. During the discharge process, VPO_4F will exhibit two discharge potential plateaus at 2.6 V ($\text{V}^{4+}/\text{V}^{3+}$) and 1.5 V ($\text{V}^{3+}/\text{V}^{2+}$) and a high theoretical specific capacity of 312 mA h g^{-1} . Meanwhile, the energy barrier for Mg^{2+} migration along the $[111]$ direction is the lowest (0.704 eV). In addition, the Mg^{2+} intercalation voltage and diffusion barriers in the analogous VPO_4O ⁹⁶ and tavorite- FeSO_4F ⁹⁷ were evaluated. VPO_4O exhibited two higher plateaus at 2.8 V and 2.2 V contributed by the higher redox couples of $\text{V}^{5+}/\text{V}^{4+}$ and $\text{V}^{4+}/\text{V}^{3+}$, and an energy barrier of about 0.58 eV along the $[111]$ direction (A–B–C) (Fig. 8b). Tavorite- FeSO_4F showed a lower diffusion energy barrier of approximately 0.36 eV along the $[010]$ direction, which is comparable to that of Li^+ migration in FeSO_4F and surpasses that of many reported RMB cathode materials (Fig. 8c). These materials are all expected to be obtained by topochemical substitution from the corresponding Li or Na salts.

Recently, our group successfully developed the high-voltage tetragonal $\text{NaV}_2\text{O}_2(\text{PO}_4)_2\text{F}/\text{reduced graphene oxide}$ (rGO) cathode material for fast and stable Mg^{2+} intercalation by topochemical extraction of two Na^+ (Na1 at the 8h site and Na2 at the 8j site) in $\text{Na}_3\text{V}_2\text{O}_2(\text{PO}_4)_2\text{F}/\text{rGO}$ (per formula) (Fig. 8d).⁹⁸ Then, Mg^{2+} was inserted into the 8h and 8j sites with a relative occupancy of 14.4% and 17%, respectively. *In situ* XRD revealed the single-phase insertion–extraction mechanism of Mg^{2+} in $\text{NaV}_2\text{O}_2(\text{PO}_4)_2\text{F}/\text{rGO}$, which is similar to the Na^+ intercalation mechanism in $\text{NaV}_2\text{O}_2(\text{PO}_4)_2\text{F}$. 1D continuous diffusion channels along the *a* direction with a diffusion energy barrier of 0.78 eV endow a high average Mg^{2+} diffusion coefficient of $2.99 \times 10^{-10} \text{ cm}^2 \text{ s}^{-1}$. Moreover, the presence of F^- ions increases the electronegativity of $(\text{PO}_4)^{3-}$, leading to a high working voltage. Benefiting from these advantages, the $\text{NaV}_2\text{O}_2(\text{PO}_4)_2\text{F}/\text{rGO}$ cathode delivered the highest average discharge voltage (3.3 V vs. Mg^{2+}/Mg) (Fig. 8e), outstanding cycling stability (97.5% capacity retention at 100 mA g^{-1}) (Fig. 8f) and remarkable rate performance (30.3 mA h g^{-1} at 5 A g^{-1}) in

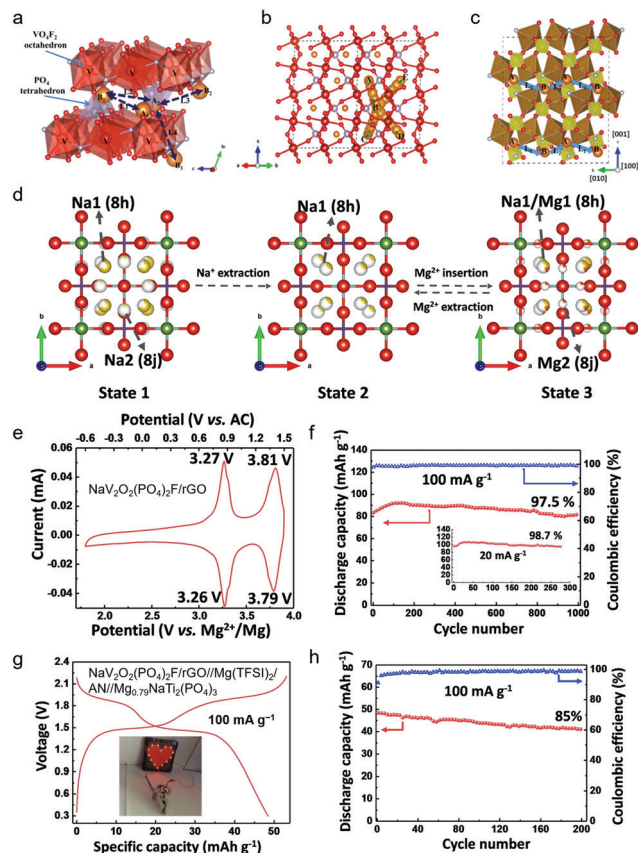


Fig. 8 The Mg^{2+} diffusion pathways in MgVPO_4F (a), VPO_4O (b) and tavorite- FeSO_4F (c) (reproduced from ref. 95–97, with permission from the Royal Society of Chemistry). (d) A schematic of topochemical substitution in $\text{Na}_3\text{V}_2\text{O}_2(\text{PO}_4)_2\text{F}$. (e) CV curve of the $\text{Na}_3\text{V}_2\text{O}_2(\text{PO}_4)_2\text{F}/\text{rGO}$ cathode between 1.8 V and 3.9 V vs. Mg^{2+}/Mg at 0.1 mV s^{-1} . (f) Cycling performances of the $\text{Na}_3\text{V}_2\text{O}_2(\text{PO}_4)_2\text{F}/\text{rGO}$ cathode at 100 mA g^{-1} . Charge–discharge curve (g) and cycling performance (h) of the Mg-ion full cell (the inset shows 14 red LEDs illuminated by two Mg-ion full cells in series). Reproduced from ref. 98, with permission from Science China Press and Springer-Verlag GmbH Germany, part of Springer Nature.

$\text{Mg}(\text{TFSI})_2/\text{AN}$ electrolyte. More importantly, after assembling with the $\text{Mg}_{0.79}\text{NaTi}_2(\text{PO}_4)_3$ anode, the Mg-ion full cell displayed a discharge capacity of 48.5 mA h g^{-1} (based on the active mass of cathode and anode) with an average discharge voltage of 1.5 V at 100 mA g^{-1} (Fig. 8g). After 200 cycles, the capacity retention rate was 84.7% (Fig. 8h). The Mg-ion full cell has room for further improvement by matching with an anode with lower potential and higher capacity. These works reveal the great potential of fluorinated polyanionic salt cathode materials for future high-energy and high-power RMBs. Besides, borate-based polyanions are also promising systems for RMBs since the inductive effect and low mass/charge ratio of borate groups endow a high operating voltage and energy density.⁹⁹

In summary, the current studies on topochemical substitution for RMB cathode materials can be mainly classified into two categories. One is electrochemical extraction and intercalation of the A-site ion in the corresponding electrolytes, which can accurately control the ion concentration and avoid the interference of the air environment. Another is the chemical

oxidation reaction between the original materials and strong oxidizing agents, such as I_2 , NOBF_4 or NO_2BF_4 , and the following reduction by $\text{Mg}(\text{C}_4\text{H}_9)_2$. This option avoids complex battery handling, and the introduction of binders and conductive additives. Topochemical substitution as a room-temperature method can moderately prepare some unique metastable phases with remarkable performance and avoid the formation of an impurity phase in high-temperature reaction. It also possesses wide universality for many insertion-type materials. But topochemical substitution can only release the inherent ion channels and sites of original crystal structures. Therefore, other methods, such as substitution doping, interlayer regulation and so forth, are necessary to modify the compositions and structures of materials.

3. Substitution doping

Substitution doping is an effective method to modify the physical or chemical properties of materials by introducing heterogeneous atoms at a specific lattice site. Generally, substitution doping changes the energy band structure, carrier density and localized electron configuration, rendering increased electron/ion conductivity or bond polarization, further enhancing the electrochemical rate performance or potential of materials. Meanwhile, it may also introduce some negative effects, such as increased side reactions or reduced structure stability. In this section, the effects of cation doping and anion doping on RMB cathode materials will be discussed and summarized.

3.1. Cation doping

The transition metal cation is usually the redox center of electrode materials, which largely determines the redox potential and electron transfer number. In conventional transition metal compounds, some similar ions can be doped in the M site to adjust the redox potential and improve the electron conductivity. Zhou *et al.* prepared Fe^{2+} doped cubic NiSe_2 ($\text{Ni}_{0.75}\text{Fe}_{0.25}\text{Se}_2$) microflowers through a facile solvothermal approach.¹⁰⁰ The Fe^{2+} ion occupies the Ni^{2+} site with 1/4 probability, owing to their close ionic radius. Compared with the single discharge voltage at $\sim 0.85 \text{ V}$ of NiSe_2 , $\text{Ni}_{0.75}\text{Fe}_{0.25}\text{Se}_2$ exhibited two clearly distinguished peaks at 0.72 and 1.03 V, revealing a stepwise electrochemical conversion process (Fig. 9a and b). As demonstrated by *ex situ* XPS, the first peak at 1.03 V was mainly contributed by the reduction from Fe^{2+} to Fe^0 , while the second peak at 0.72 V resulted from the reduction of Ni^{2+} (Fig. 9c). This indicated that the doping of Fe^{2+} increases the potential of the whole material based on the $\text{Fe}^{2+}/\text{Fe}^0$ redox couple. Moreover, the precipitated Fe metal enhances the electron conduction of electrode materials. Then, the defect-rich NiSe_2 possesses broadened ion channels that allow faster Mg^{2+} diffusion kinetics (Fig. 9d).

The effect of M-site cation doping in insertion-type cathode materials on accelerating Mg^{2+} diffusion or hopping at different sites is more obvious.¹⁰¹ Spinel $\text{Li}_4\text{Ti}_5\text{O}_{12}$ as a “zero strain” insertion material has been widely investigated for LIBs. When applied as the host material for Mg^{2+} intercalation,

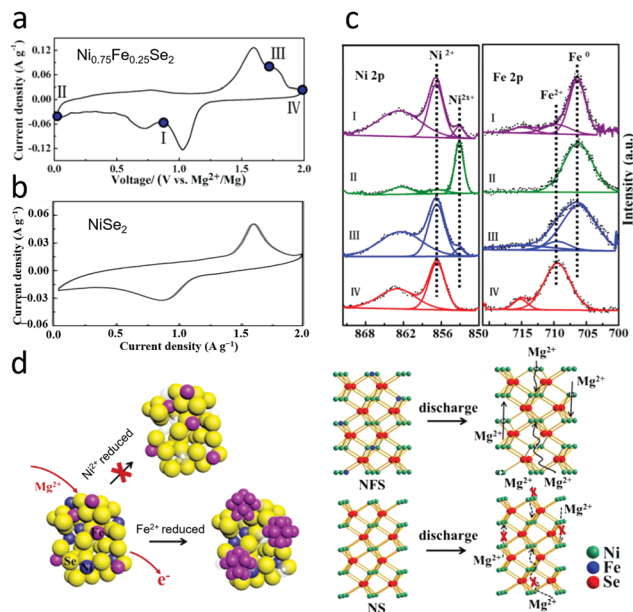


Fig. 9 CV curves of the $\text{Ni}_{0.75}\text{Fe}_{0.25}\text{Se}_2$ (a) and NiSe_2 (b) electrode at 0.5 mV s^{-1} . (c) *Ex situ* XPS spectra of $\text{Ni}_{0.75}\text{Fe}_{0.25}\text{Se}_2$ at different voltages. (d) Schematic of the electrochemical reaction mechanism of $\text{Ni}_{0.75}\text{Fe}_{0.25}\text{Se}_2$ and NiSe_2 . Reproduced from ref. 100, with permission from Elsevier.

it underwent a multi-phase transformation mechanism from $\text{Li}_4\text{Ti}_5\text{O}_{12}$ to $\text{Mg}_x\text{LiTi}_5\text{O}_{12}$ and $\text{Li}_7\text{Ti}_5\text{O}_{12}$.⁷¹ After full charging, the co-extraction of Mg^{2+} and Li^+ induced the formation of $\text{Mg}_{2.5}\text{LiTi}_5\text{O}_{12}$ as the final active structure for the following cycles. The activation process from $\text{Li}_4\text{Ti}_5\text{O}_{12}$ to $\text{Mg}_{2.5}\text{LiTi}_5\text{O}_{12}$ usually requires dozens of cycles in organic electrolyte. Lee *et al.* accelerated the activation process by the doping of trivalent Cr^{3+} in nano $\text{Li}_4\text{Ti}_5\text{O}_{12}$ ($\text{Li}_{3.91}\text{Cr}_{0.26}\text{Ti}_{4.82}\text{O}_{12}$), where three Cr^{3+} replaced one Li^+ and two Ti^{4+} at 16d sites simultaneously.¹⁰² Meanwhile, this significantly enhanced the discharge capacity and rate performance of $\text{Li}_4\text{Ti}_5\text{O}_{12}$ by increasing electrical conductivity and structural disorder (Fig. 10a and b). As demonstrated by DFT calculations, the diffusion energy barriers of Li^+ and Mg^{2+} (8a–16c–8a) in Cr-doped $\text{Li}_4\text{Ti}_5\text{O}_{12}$ were lower than those in $\text{Li}_4\text{Ti}_5\text{O}_{12}$ (Fig. 10c–e). The enhanced ion diffusion facilitated the migration of the multiphase interface during ion intercalation/de-intercalation, thereby accelerating the activation process, while improving the rate performance of $\text{Li}_4\text{Ti}_5\text{O}_{12}$ for Mg^{2+} storage.

Furthermore, cation doping can improve the structure stability of cathode materials, especially for Mn-based spinel and layered oxides. Owing to the Jahn–Teller distortion of high-spin Mn^{3+} in MnO_6 octahedron and its serious dissolution in aqueous electrolyte, Mn-based spinel and layered oxides usually undergo a rapid capacity fading.¹⁰³ The doping of inactive or low-valence metal atoms in the Mn site, such as Mg, Fe, Ti, Al, Ni, Co, Cr, Mo, and so forth, can stabilize the crystal framework or reduce the formation of Mn^{3+} , resulting in an improved cycling performance. Zhang *et al.* investigated the Mg^{2+} storage performances of $\text{MgFe}_x\text{Mn}_{2-x}\text{O}_4$ with an increased Fe/Mn ratio in aqueous MgCl_2 electrolyte.¹⁰⁴ When the ratio of Fe/Mn is 2:1, the optimal discharge capacity of $136.5 \text{ mA h g}^{-1}$ at

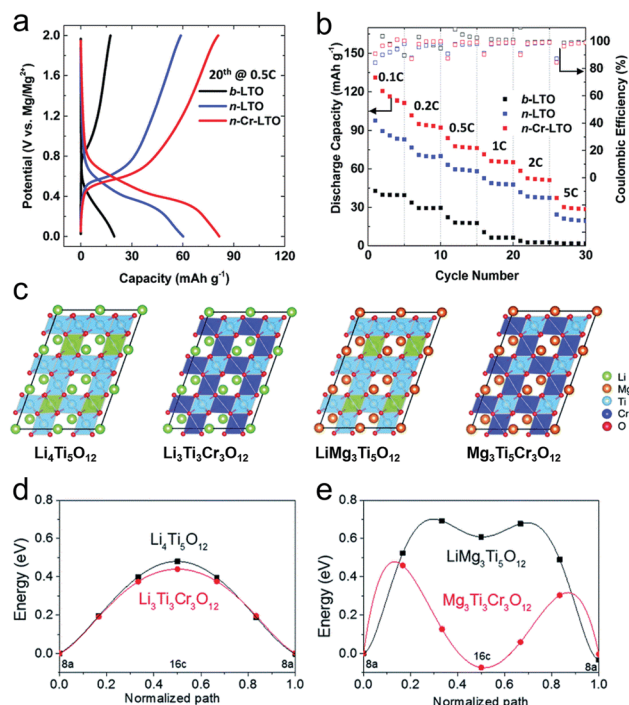


Fig. 10 (a) Discharge–charge curves for the 20th cycle and (b) rate performances of bulk-type $\text{Li}_4\text{Ti}_5\text{O}_{12}$ (b-LTO), nano-sized $\text{Li}_4\text{Ti}_5\text{O}_{12}$ (n-LTO), and Cr-doped $\text{Li}_4\text{Ti}_5\text{O}_{12}$ nanocrystal (n-Cr-LTO) at 0.5C ($1\text{C} = 175 \text{ mA h g}^{-1}$). (c) Crystal structures of $\text{Li}_4\text{Ti}_5\text{O}_{12}$, $\text{Li}_3\text{Ti}_3\text{Cr}_3\text{O}_{12}$, $\text{LiMg}_3\text{Ti}_5\text{O}_{12}$ and $\text{Mg}_3\text{Ti}_3\text{Cr}_3\text{O}_{12}$ and the corresponding diffusion energy barriers of Li^+ (d) and Mg^{2+} (e) between tetrahedral 8a sites via the octahedral 16c site. Reproduced from ref. 102, with permission from the Royal Society of Chemistry.

50 mA g^{-1} and cycling stability (88.3 mA h g^{-1} after 1000 cycles at 1 A g^{-1}) are achieved. Unfortunately, the related works on cation doping for high-energy RMB cathode materials, such as spinel compounds, layered oxides, olivine silicates and so forth, have rarely been reported.

3.2. Anion doping

Introducing anions with higher polarizability into the anion lattice of materials is an effective way to decrease the electrostatic interactions between Mg^{2+} and the anion lattice, thereby reducing the barriers for Mg^{2+} diffusion. For example, in the chalcogenide group, the polarizability of chalcogenide ions gradually increases with the increase of the ionic radius and reduction of electronegativity ($\text{Te}^{2-} > \text{Se}^{2-} > \text{S}^{2-} > \text{O}^{2-}$).¹⁰⁵ The high-polarizability atom can deform the electronic charge density of the anion lattice during Mg^{2+} shuttling, owing to a decreased binding force of the nucleus to the bound electron. This is also interpreted as the deformability of the electron clouds of the anionic framework. Upon the intercalation of Mg^{2+} , the high deformability can easily accommodate the brought charge, further facilitating Mg^{2+} mobility. Especially in the layered MX_2 structures ($\text{M} = \text{Ti}, \text{V}; \text{X} = \text{O}, \text{S}, \text{Se}$), the above rule is obvious owing to the direct interaction between the 2D anion layer and Mg^{2+} . Charge rehybridization further verified this rule upon Mg^{2+} diffusion between the interlayers of MX_2 .¹⁰⁶

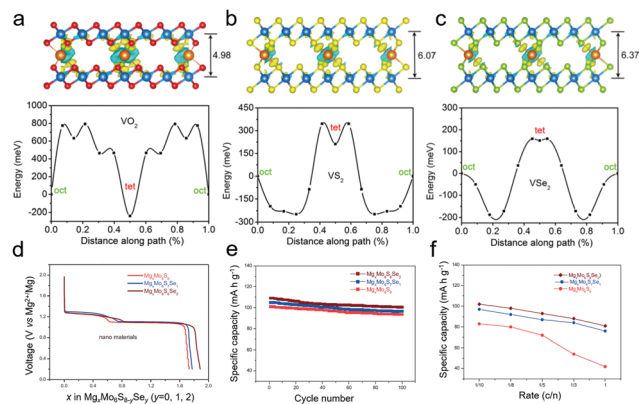


Fig. 11 Charge rehybridization and diffusion barriers upon Mg^{2+} diffusion between interlayers of (a) VO_2 , (b) VS_2 , and (c) VSe_2 . Reproduced from ref. 106, with permission from the American Chemical Society. Discharge curves (d), cycling (e) and rate performances (f) of various $\text{Mo}_6\text{S}_{8-y}\text{Se}_y$ ($0 < y < 2$) phases. Reproduced from ref. 109, with permission from Wiley-VCH.

In Fig. 11a–c, the yellow color signifies charge accumulation, while blue signifies depletion of electron density. Obviously, along with the increased polarizability from O^{2-} to Se^{2-} , the charge rehybridization gradually decreased, which indicates the increasing charge deformability.^{107,108} Combined with the reduced Mg^{2+} diffusion barriers from 1032 to 593 to 346 meV in the series of “O–S–Se”, the higher polarizability truly accounted for the faster Mg^{2+} migration in the interlayer of MX_2 . In addition, the expanded diffusion channel and increased electron conductivity promote Mg^{2+} storage and diffusion kinetics in layered MSe_2 materials. The effect of Se doping was confirmed in the Chevrel Mo_6S_8 phase. With the increased content of Se substitution doping from 0 to 2 in the $\text{Mo}_6\text{S}_{8-y}\text{Se}_y$ ($0 \leq y \leq 2$) phase, the discharge capacity increased gradually and the rate performance was improved dramatically (Fig. 11d–f).¹⁰⁹ The presence of Se not only increased the polarizability of the anion framework, but it also changed the geometry of Mg insertion sites (the inner and outer rings), which resulted in a more facile Mg^{2+} hopping in these sites, thus enhancing the reaction kinetics. In spite of the fact that the introduction of Se lowered the theoretical specific capacity, an enhanced ion/electron transformation kinetics endowed a higher practical capacity. In addition, in conversion-type CuS cathode materials, the anionic Se substitution also improved the redox reaction kinetics and electrical conductivity.¹¹⁰

The polarizability of the anion lattice is also related to the types of covalent bonds to some degree. The F^- ion with lower polarizability than O^{2-} usually increases the intercalation energy of Mg^{2+} , thus improving the redox potential of electrode materials. It is also capable of decreasing the electrostatic interaction between Mg and anions in specific crystal frameworks, facilitating Mg^{2+} diffusion. Incorvati *et al.* studied the effects of mild F^- doping in layered $\alpha\text{-MoO}_3$ for Mg^{2+} intercalation.¹¹¹ The obtained $\text{MoO}_{2.8}\text{F}_{0.2}$ maintained the layered structure and showed dramatically improved specific capacity and capacity retention, compared to the isostructural $\alpha\text{-MoO}_3$,

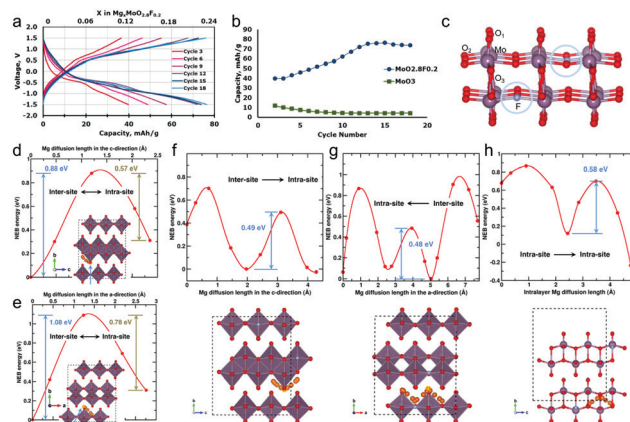


Fig. 12 Charge–discharge curves (a) and cycling stability (b) of $\text{MoO}_{2.8}\text{F}_{0.2}$. (c) The three types of oxygen in the MoO_6 octahedron and the optimal configuration of F doping in $\alpha\text{-MoO}_3$. Calculated Mg diffusion energies through the $\alpha\text{-MoO}_3$ lattice (d, e) and F doped $\alpha\text{-MoO}_3$ (f–h). Reproduced from ref. 111 and 112, with permission from the American Chemical Society.

(Fig. 12a and b). In the MoO_6 octahedron, three types of oxygen atoms, $\text{O}_{(1)}$, $\text{O}_{(2)}$, and $\text{O}_{(3)}$, were denoted. The $\text{Mo}\text{--}\text{O}_2$ bond exhibits two distinctly different bond lengths, resulting from the strong cation–cation distortion (Fig. 12c).¹¹² As demonstrated by DFT calculations, F tends to replace the O_2 atom owing to the lowest energetic cost. Interestingly, the displacement of F in O_2 sites homogenizes the $\text{Mo}\text{--}\text{F}/\text{Mo}\text{--}\text{O}_2$ bond length, reducing the cation–cation distortion and largely decreasing the electronic band gap, thus enhancing the electron conductivity. When increasing the content of F^- , one or two F atoms will occupy the O_2 sites while homogeneously dispersing among the $\text{Mo}\text{--}\text{O}$ layers in a typical $3 \times 1 \times 3$ supercell (Fig. 12c). Upon Mg^{2+} diffusion, compared to the high energy barriers of at least 0.88 eV from interlayer to intralayer sites in $\alpha\text{-MoO}_3$ (Fig. 12d and e), Mg^{2+} only needs to overcome a low energy barrier of 0.5 eV in F doped $\alpha\text{-MoO}_3$ (Fig. 12f–h). In addition, F doping did not decrease the formation energy for Mg^{2+} intercalation. Consequently, the redox potential of F doped $\alpha\text{-MoO}_3$ is similar to that of $\alpha\text{-MoO}_3$.

Substitution doping has undergone great developments in materials science and has been applied widely in various energy storage and conversion fields. Due to its versatility, it has enormous potential for simultaneously improving the working voltage, specific capacity, rate performance and even structure stability. Unfortunately, the related reports in the RMB field are relatively few, and vast attempts should be made. Moreover, compared to single atom doping, multi-atom doping in one crystal system by cations and anions could combine their advantages and may synchronously increase the redox potential, ion diffusion kinetics and structure stability. But this may be at the expense of a complicated process and high cost.

4. Interlayer regulation

A lot of layered materials have also been reported for RMBs, such as transition-metal dichalcogenides (TMDs)^{113–116}

(MoS₂, VS₂, TiS₂, WS₂, TiSe₂, and VSe₂), transition-metal oxides or polyanionic salts^{117–126} (bilayered V₂O₅, α -V₂O₅, H₂V₃O₈, MoO₃, birnessite MnO₂, V₂MoO₈, and tetragonal VOPO₄), MXenes¹²⁷ (Ti₂C, Ti₃C₂, and V₂C) and so forth.^{25,128,129} However, the strong interaction between Mg²⁺ and anions still results in a sluggish migration of Mg²⁺ in layered host materials, especially for the strong interaction between bivalent Mg²⁺ and the O element. This was also verified by first-principles nudged elastic band (NEB) calculation on α -V₂O₅ (activation barrier of 975–1100 meV).¹³⁰ The above-mentioned anion substitution (Section 2.2.2) effectively reduces the Mg²⁺ migration barriers in layered metal oxides by reducing electrostatic interactions between Mg²⁺ and the anion lattice. However, anion substitution by ions with high polarizability can usually decrease the redox potentials and specific capacity for Mg intercalation in 2D materials, thus lowering the energy density of RMBs.

Interlayer regulation is another effective method to facilitate Mg²⁺ diffusion in layered materials by introducing pillared ions or molecules (Fig. 13). The inserted pillared ions and molecules in the interlayer can controllably expand or shrink the interlayer distance, thereby reducing the Mg²⁺ diffusion barrier or stabilizing the layer structure. In addition, the pillared molecules with high polarity are able to shield the strong interaction from the host materials by a nucleophilic reaction with Mg²⁺, thus improving Mg²⁺ migration. In this section, the functions, optimization mechanisms and development processes of various pillared units in the interlayers of various 2D layered materials for RMBs are systematically discussed, based on four categories of water, metal ion and organic molecule regulation and solvent co-intercalation.

4.1. H₂O molecule insertion

The H₂O molecule with a strong polar dipole easily solvates Mg²⁺ to form the hydrated Mg(H₂O)₆²⁺ ion, which is able to shield the strong polarization of Mg²⁺ and further reduce the interaction from host materials during the ion diffusion process. This discovery originates from inchoate Mg²⁺ intercalation studies in V₂O₅ xerogel in the 1990s.^{131,132} The high specific capacity and favorable rate performance of V₂O₅

xerogel for Mg²⁺ storage compared to those of orthorhombic V₂O₅ attracted the attention of a wide range of scholars. Subsequently, lots of improvement works, including the introduction of high-conductive carbon,^{133,134} current collectors,¹³⁵ or optimizing the electrolyte components,^{136,137} were reported in succession. But the role of the interlayer H₂O molecule in the Mg²⁺ intercalation mechanism in V₂O₅ still lacks deep experimental characterization.

In 2015, Tepavcevic *et al.* revealed the evolution of the layered structure of V₂O₅ xerogel (bilayered V₂O₅) during discharge/charge processes by using small-angle and wide-angle X-ray scattering.¹¹⁷ Upon Mg²⁺ intercalation, the lattice parameter *c* of bilayered V₂O₅ decreased from 13.1 Å to 11.0 Å without significantly changes in the lattice parameters *a* and *b*, which indicates that Mg²⁺ only intercalates in the interlayer of bilayered V₂O₅ and the strong interaction between bivalent Mg ions and terminal hydroxyl groups results in the shrinkage of layer spacing. This was also verified by molecular dynamics (MD) simulation. Meanwhile, MD simulations showed a significant solvation process between the inserted Mg ions and the remaining water molecules in the structure. Moreover, a full Mg ion battery assembled by the Mg_xV₂O₅/CNF cathode, Sn anode and Mg(ClO₄)₂/AN electrolyte was firstly designed. It showed reversible Mg intercalation with a discharge capacity of 160 mA h g⁻¹ at 20 mA g⁻¹ and an average voltage of ~0.6 V, but limited cycling and rate performances. In addition, an excess Sn anode is required and dissolution of Sn in the electrolyte was observed. During the same period, our group significantly improved the cycling stability and rate performance by loading the V₂O₅ xerogel nanowire on graphene (VOG).¹³⁸ The VOG composite also exhibited a broad working temperature window from -30 °C to 55 °C with a capacity over 200 mA h g⁻¹ at 55 °C (1.0 A g⁻¹). Meanwhile, the average diffusivity of Mg²⁺ in the interlayer of V₂O₅ xerogel was calculated as 3 × 10⁻¹¹ cm² s⁻¹ based on GITT. This is about one order of magnitude higher than the Mg²⁺ diffusivity in Chevral phase Mo₆S₈ (2–6 × 10⁻¹² cm² s⁻¹).³⁹ Further, the control electrochemical experiments for the VOG composite with different H₂O contents demonstrated that the interlayer H₂O molecule plays a critical role in reducing the diffusion barrier and increasing the magnesian concentration by shielding the polarization of Mg ions.

In spite of this, there were no theoretical studies that demonstrated the role of interlayer water in the bilayered V₂O₅ system upon Mg ion intercalation under different solvent conditions. On the other hand, it is uncertain whether the interlayer H₂O in bilayered V₂O₅ shuttles along with Mg²⁺ after solvation in various electrolytes and at different Mg concentrations. Ceder and coworkers deeply investigated the subject by using first-principles calculations in 2016.¹³⁹ The Mg coordination environment in Mg_{0.5}V₂O₅·H₂O was recognized as the hexa-coordinate structure, where each Mg is bonded to four O^w atoms from interlayer H₂O and two O atoms of the VO_x polyhedra (Fig. 14a). The dashed lines in the figure represent hydrogen bonds between H₂O molecules and the lattice O_x. Upon Mg removal, the stronger hydrogen bond energy between H₂O would lead to a stable

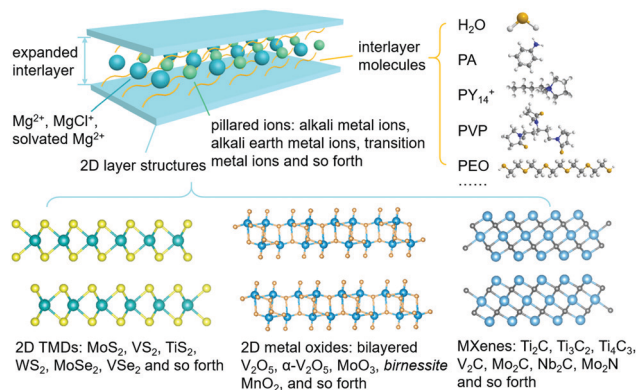


Fig. 13 Overview of the various interlayer additives, including metal ions, H₂O and organic molecules in reported 2D layered RMB cathode materials.

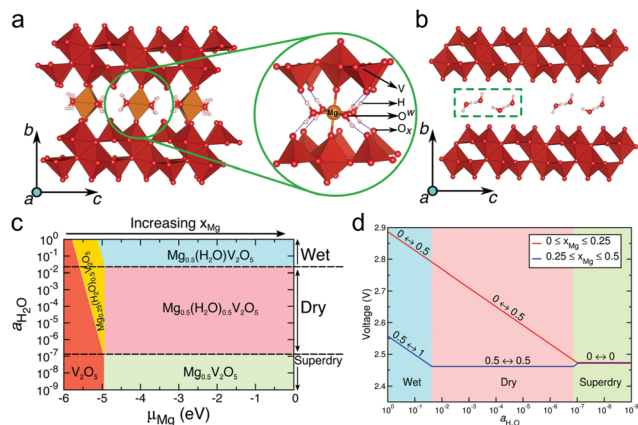


Fig. 14 Crystal structures of the fully magnesiated ($x_{\text{Mg}} = 0.5$) and the fully demagnesiated $\text{V}_2\text{O}_5 \cdot n\text{H}_2\text{O}$ (a and b). (c) Grand-potential phase diagram at 0 K of Mg-xerogel V_2O_5 as a function of various electrolytes and Mg chemical potentials (μ_{Mg}). $\mu_{\text{Mg}} = 0$ corresponds to full magnesiation. (d) Average Mg insertion voltage as a function of water content in the electrolyte at low (red line) and high (blue) Mg concentrations. Reproduced from ref. 139, with permission from the American Chemical Society.

arrangement of H_2O molecules in the interlayer (Fig. 14b). Then, the phase diagrams at 0 K and different voltages as a function of both Mg and H_2O concentration in the structure were presented, based on a lot of DFT calculations (Fig. 14c and d). The diagram was divided into three regimes by the water activity ($a_{\text{H}_2\text{O}}$), where “wet” is ~ 1 , “dry” is from 10^{-2} to 10^{-6} , and “superdry” is $< 10^{-7}$. A higher Mg chemical potential (μ_{Mg}) refers to a higher Mg content in the V_2O_5 xerogel. According to Fig. 14c, it was found that Mg^{2+} shuttles along with H_2O molecules across the interlayer of bilayered V_2O_5 under wet conditions, whereas under dry conditions, water would not shuttle with Mg^{2+} . Further, the presence of interlayer H_2O molecules could increase the voltage for Mg intercalation, especially in wet electrolytes (Fig. 14d). This was also confirmed by experimental studies. A higher initial voltage (~ 3.02 V) in aqueous electrolyte could be observed, compared to that at ~ 2.88 V and ~ 2.35 V in dry and nonaqueous electrolytes, respectively.

Soon afterward, Sa and Ceder *et al.* presented a more in-depth Mg^{2+} insertion mechanism in the $\text{V}_2\text{O}_5 \cdot n\text{H}_2\text{O}$ xerogel in dry electrolyte ($\text{Mg}(\text{TFSI})_2$ dissolved in diglyme).¹¹⁹ They thought that the diglyme-solvated Mg^{2+} can co-intercalate into the bilayered $\text{V}_2\text{O}_5 \cdot n\text{H}_2\text{O}$ interlayer and largely shed the lattice water. Meanwhile, the co-intercalation of diglyme is reversible upon magnesiation/de-magnesiation processes. Interestingly, after co-deintercalation of diglyme-solvated Mg^{2+} , diglyme molecules would fill the bilayered $\text{V}_2\text{O}_5 \cdot n\text{H}_2\text{O}$ that serves as a “reservoir”. This mechanism is achieved at the expense of further decomposition of the electrolyte and passivation of the Mg metal due to the removal of lattice H_2O and the decomposed electrolyte species. In 2018, Wang and coworkers further investigated the role of H_2O in Mg^{2+} intercalation in 2D layered materials using the layered $\text{VOPO}_4 \cdot n\text{H}_2\text{O}$ as a model material.¹²⁰ The dry and wet electrolytes were prepared by dissolving 0.1 M $\text{Mg}(\text{ClO}_4)_2 \cdot 6\text{H}_2\text{O}$ and $\text{Mg}(\text{ClO}_4)_2$, respectively,

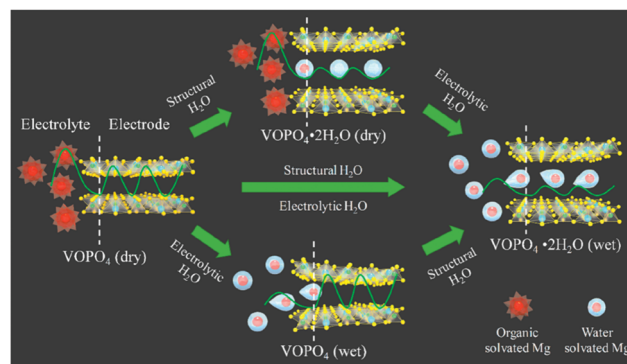


Fig. 15 Schematic of the solvated Mg^{2+} storage mechanisms in $\text{VOPO}_4 \cdot n\text{H}_2\text{O}$ in dry and wet electrolytes (green curves: activation energy barriers; white dashed lines: electrolyte/electrode interface). Reproduced from ref. 120, with permission from the American Chemical Society.

in propylene carbonate (PC). Under the wet condition, the same conclusion that the interlayer H_2O shields the polarization of Mg^{2+} and increases the working voltage was proposed (Fig. 15). The different opinion was that a desolvation step of $\text{Mg}(\text{PC})_6^{2+}$ would occur at the electrolyte/cathode interface before Mg^{2+} insertion in $\text{VOPO}_4 \cdot n\text{H}_2\text{O}$ under dry conditions. Subsequently, Mg^{2+} inserted into the $\text{VOPO}_4 \cdot n\text{H}_2\text{O}$ interlayer and was further solvated by H_2O molecules for fast migration. During the charge process, the interlayer H_2O molecules would be extracted accompanied by Mg^{2+} deintercalation.

In summary, the actual roles of interlayer H_2O in the two processes of Mg^{2+} intercalation and deintercalation in layered materials are still controversial and ambiguous. Especially in organic electrolyte, the following issues still need plenty of research and discussion. (1) Can the organic-solvated Mg^{2+} co-intercalate into the interlayer of 2D hydrated layered materials? (2) Will the interlayer H_2O shuttle into the organic electrolyte accompanied by Mg^{2+} ? The answers should depend on several factors, including the desolvation energy of organic-solvated (G_{organic}) and hydrated Mg^{2+} (G_{water}), the interlayer distance (decided by the H_2O content) and the anion electronegativity of the layered materials. When $G_{\text{organic}} > G_{\text{water}}$ and the diameter of organic-solvated Mg^{2+} is lower than the interlayer distance, organic-solvated Mg^{2+} may tend to reversibly intercalate/de-intercalate into layered materials. Meanwhile, the insertion of free organic molecules into the hydrated interlayer possibly occurs owing to the acid–base proton reaction. When $G_{\text{water}} > G_{\text{organic}}$, organic-solvated Mg^{2+} may tend to de-solvate at the electrode/electrolyte interface, further combine with the interlayer H_2O to diffuse in the host material and shuttle into the electrolyte. So, we think that the polarity, configuration of the organic solvent and the interlayer H_2O content significantly determine the Mg^{2+} intercalation/de-intercalation behaviors. This needs deeper and broader investigations, and even statistics to promote the development of 2D hydrated materials for RBMs.

4.2. Organic molecule regulation

In order to avoid the H_2O -shuttling-induced surface passivation of the Mg metal anode, interlayer organic molecule regulation

as a more feasible strategy was gradually developed for RMB applications. Some usual polymer ligands,^{140–142} (polyethylene oxide (PEO) and polyvinylpyrrolidone (PVP)), nucleophilic molecules¹⁴³ (phenylamine (PA)), and organic cations^{144–146} (1-butyl-1-methylpyrrolidinium ion (PY₁₄⁺) and cetyltrimethylammonium ion (CTA⁺)) were employed to expand the interlayer spacing of TMDs, layered oxides or MXenes and thus decrease Mg²⁺ diffusion barriers.

Yao and coworkers firstly constructed the PEO-expanded MoS₂ structure *via* exfoliation of MoS₂ bulk, followed by restacking of PEO ligands and single-layer MoS₂.¹⁴⁰ The interlayer distance could be increased to 1.19 nm (PEO-MoS₂) and to even 1.45 nm (PEO₂-MoS₂) with 0.49 and 1.00 molar PEO in MoS₂, respectively, whereas that of H₂O-inserted MoS₂ (0.98 molar) was just 0.633 nm. The largely expanded interlayer spacing truly allowed faster Mg²⁺ diffusion, in which the average Mg diffusivity in PEO₂-MoS₂ was twice that in H₂O-inserted MoS₂. PEO₂-MoS₂ also delivered a specific capacity double that of H₂O-inserted MoS₂ in APC electrolyte. However, the further expanded interlayer spacing is not more beneficial for Mg-ion storage, while the interlayer composition also affects the Mg-ion storage performance. High amounts of polymer ligands may occupy the Mg²⁺ sites, reducing the Mg²⁺ migration rate and storage capacity.¹⁴¹ Meanwhile, high amounts of polymer will lower the electronic conductivity of host materials owing to its insulativity. Therefore, choosing short organic chains as the “pillar” unit may reasonably avoid the issues while increasing the interlayer spacing. Yao and coworkers further employed the PY₁₄⁺ chain to expand the moisture-sensitive TiS₂ by an *in situ* electrochemistry intercalation for preventing oxidation (Fig. 16a).¹⁴⁴ After the first discharge to 1 V (stage 1), the interlayer distance could be expanded to 10.86 Å. Then, the active MgCl⁺ species would insert into the interlayer; this mechanism was proposed in halogen-containing Mg electrolytes for the first time. This phenomenon is primarily due to the fact that the energy (> 3 eV) for breaking the Mg–Cl bond and the

diffusion energy barrier (> 1 eV) of Mg²⁺ largely exceed the energy barrier (0.18 eV) of low-polarization MgCl⁺ in expanded TiS₂. More importantly, the expanded layer spacing (18.63 Å) by intercalation of PY₁₄⁺ further facilitated the fast diffusion of MgCl⁺. Benefitting from these advantages, the average diffusivity of MgCl⁺ reached 10^{–11} cm² s^{–1}, and the expanded TiS₂ exhibited a high specific capacity of over 300 mA h g^{–1} (Fig. 16b). At stage 3 (0 V), the layer structure of MgCl⁺ inserted TiS₂ would undergo distortion, but the distortion does not lead to structure collapse or shuttling of pillared PY₁₄⁺, thus a long cycling life at 240 mA g^{–1} could be obtained (Fig. 16c).

With regard to some hydrated layered compounds, the *in situ* electrochemical insertion of organic ions may be infeasible owing to possible H₂O shuttling. In this case, a nucleophilic organic molecule could be intercalated as a short chain “pillar” unit by a nucleophilic reaction with lattice H₂O or by displacement. Our group chose hydrated VOPO₄ (OH-VOPO₄) as a model material; the PA intercalated VOPO₄ nanosheets (PA-VOPO₄) were prepared by a displacement reaction.¹⁴³ PA-VOPO₄ delivered a largely increased discharge capacity of 310 mA h g^{–1} at 100 mA g^{–1} compared to ~160 mA h g^{–1} of OH-VOPO₄, and a long cycle life (192 mA h g^{–1} after 500 cycles). The optimized performance was contributed by the enlarged layer distance of 1.424 nm and a fast MgCl⁺ diffusion (Fig. 17a). Interestingly, the diffusion routine and energy barriers of Mg²⁺ and MgCl⁺ in PA-VOPO₄ were calculated by DFT (Fig. 17b and c). In Path 1, the diffusion energy barrier of MgCl⁺ (0.42 eV) is the lowest, relative to the others.

These works further reveal that the synergistic effect of MgCl⁺ intercalation and organic-expanded diffusion spacing opens a door for the development of high-rate and high-capacity RMB cathodes. The strategy, organic molecule regulation, was also widely applied to other 2D materials, such as Ti₂C₃,¹²⁷ VS₂¹⁴⁶ and so forth.

4.3. Co-intercalation of Mg²⁺ and solvent

The pre-intercalation of H₂O or organic molecules in layered structures suggests the feasibility of co-intercalation of Mg²⁺

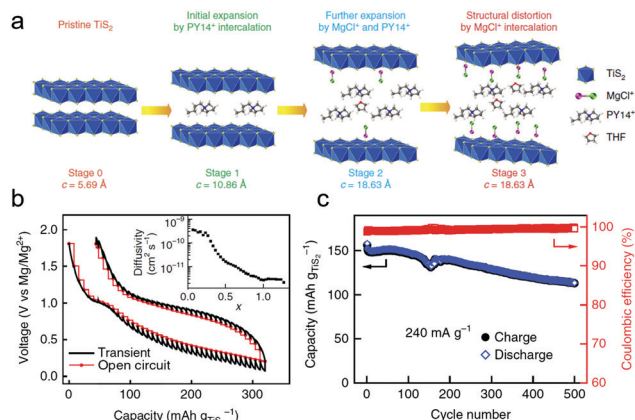


Fig. 16 (a) A schematic of the structural evolution of TiS₂ at different discharge stages: original state (Stage 0), and discharge to 1.0 V (Stage 1), 0.2 V (Stage 2) and 0 V (Stage 3). (b) GITT curve of expanded-TiS₂. (c) Cycling performance at 1C (240 mA g^{–1}). Reproduced from ref. 144, with permission from Nature Publishing Group.

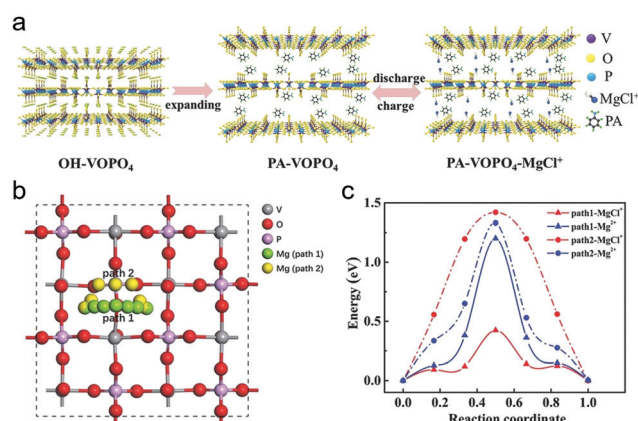


Fig. 17 (a) Schematic illustration of the expanded PA-VOPO₄ nanosheets for MgCl⁺ intercalation. Diffusion routine (b) and energy barrier profiles (c) of Mg²⁺/MgCl⁺ transport in the PA-VOPO₄ interlayer. Reproduced from ref. 143, with permission from Wiley-VCH.

and solvent during magnesian/demagnesian processes. The intercalation of the solvated Li^+ or Na^+ ion in layered materials, quasi-layered materials and even non-layered materials has been found and discussed in LIBs and SIBs.¹⁴⁷ It primarily occurs in the following cases: (1) the intercalation of the pure metal ion in the host is thermodynamically unfavorable, such as in the well-known example of the intercalation of Na^+ into graphite.¹⁴⁸ (2) A too high intercalation energy barrier of the pure metal ion or a too high desolvation energy of the solvated ions leads to sluggish kinetics, which mainly occurs in multivalent ion intercalation processes or in high-polarity electrolyte systems.¹⁴⁹ In these cases, the co-intercalation of ion and solvent may be more thermodynamically and kinetically favorable. Especially for Mg intercalation chemistry, the solvated Mg^{2+} ions have a larger ionic radius and thus reduced charge density, resulting in a lower migration energy barrier through the host, which is also referred to as the “shielding effect”.

In aqueous magnesium ion batteries (AMIBs), water co-intercalation can take place easily. The strong shielding effect of water molecules can significantly enhance the intercalation and diffusion kinetics. This provides new opportunities for the fast development of AMIBs. The intercalation mechanisms of $\text{Mg}(\text{H}_2\text{O})_6^{2+}$ in bilayered $\text{V}_2\text{O}_5 \cdot n\text{H}_2\text{O}$ and $\text{VOPO}_4 \cdot n\text{H}_2\text{O}$ have also been discussed in Section 4.1. For organic RMBs, Kim *et al.* first presented the co-intercalation of Mg^{2+} and linear ether solvents into graphite.¹²⁸ Compared to ethylene carbonate (EC) and diethylene carbonate (DEC) solvents, the binding energies between Mg^{2+} and ether solvents, such as DME and diethylene glycol dimethyl ether (DEGDME), are higher, which indicates that the solvation of Mg^{2+} by linear ether solvents is most energetically favorable. Meanwhile, DFT, *ex situ* XRD and Fourier transform infrared spectroscopy (FT-IR) analyses demonstrated that the intercalation and diffusion of double-layer Mg^{2+} /DEGDME into and through graphite are thermodynamically and kinetically favorable. Fichtner and co-workers further developed the co-intercalation chemistry into the MoS_2 cathode for RMBs.¹¹⁵ In the magnesium tetrakis(hexafluoroisopropoxy)borate (MgBOR)/DME electrolyte, the porous 2H- MoS_2 nanorods delivered a high capacity of 120 mA h g^{-1} and exhibited a good cycling stability (retention of 71% after 200 cycles at 0.5 A g^{-1}). The STEM-EDX and pair distribution function (PDF) analyses clearly demonstrated the intercalation of the solvated Mg^{2+} ions ($[\text{Mg}(\text{DME})_3]^{2+}$) in 2D layered 2H- MoS_2 . The intercalation of large solvated Mg ions leads to the fragmentation and structural distortion of 2H- MoS_2 (Fig. 18). Meanwhile, a transition from semi-conductive 2H to metallic 1T phase would occur, which largely improved the electron conductivity. Interestingly, after the extraction of $\text{Mg}(\text{DME})_3^{2+}$, the 1T- MoS_2 fragments preferred to rearrange and transform back to the thermodynamically stable 2H phase. In addition, less DME molecules and Mg^{2+} ions would remain in the interlamination of 2H- MoS_2 , inducing an electrochemical activation of the surface structure. The co-intercalation of solvent and Mg^{2+} effectively shields the strong electrostatic interaction from the host and avoids the extra introduction of inactive interlayer molecules in RMBs, compared to other interlayer regulation strategies. This method provides a new opportunity

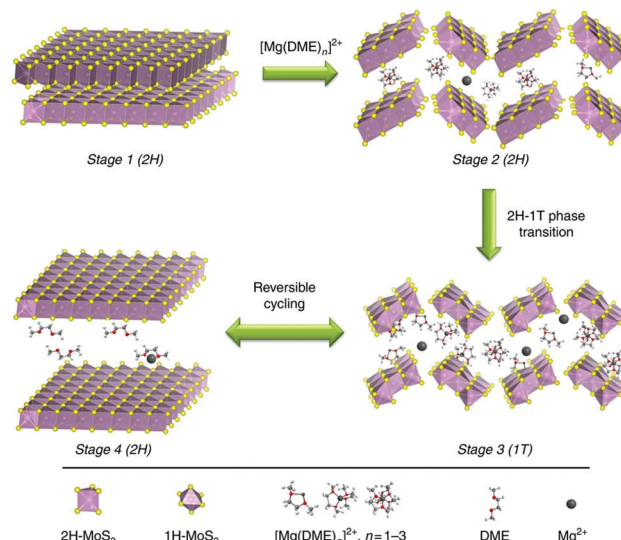


Fig. 18 Schematic illustration of the DME-solvated Mg^{2+} storage mechanism in MoS_2 structures. Reproduced from ref. 115, with permission from Nature Publishing Group.

for high-energy RMBs by employing high-energy cathode materials and highly anodically stable halogen-free electrolytes.

4.4. Pillared ion regulation

Metal ions can also be employed to modify the interlayer spacing by electrostatic interactions with the anion layer of 2D materials. Meanwhile, the electrostatic interactions can stabilize the expansion/shrinkage of the layer structure during repeated Mg^{2+} intercalation/de-intercalation. Compared with the organic molecule intercalation, metal ion regulation is able to minimize the occupying volume of the “pillar” unit. Moreover, the electrostatic repulsion between pillared metal cations and Mg ions may accelerate the migration kinetics of Mg ions in a specific path, whereas the nucleophilic groups of pillared organic molecules may interact with the diffused Mg ions.

The pillared metal ions mainly include alkali metal, alkali earth metal and transition metal ions. Monovalent alkali metal ions with low polarization readily intercalate into the layer of 2D materials. Their intercalation chemistries have also been widely studied in LIBs and other energy storage systems.¹⁵⁰ Tang *et al.* summarized the interlayer spacing change of Li, Na, and K ions in the V_3O_8 layer ($\text{A-V}_3\text{O}_8$: $\text{LiV}_3\text{O}_8 = 6.32 \text{ \AA}$, $\text{NaV}_3\text{O}_8 = 6.85 \text{ \AA}$, $\text{KV}_3\text{O}_8 = 7.48 \text{ \AA}$).¹⁵¹ The interlayer spacing gradually increased with the increased ionic radius of alkali metal ions. Upon Mg^{2+} insertion, LiV_3O_8 exhibited a higher specific capacity but a poor cycling stability. In contrast, KV_3O_8 delivered a low specific capacity but a high cycling stability. The performance of NaV_3O_8 was in-between. These results indicated that the alkali metal ions with a large ionic radius occupy more Mg^{2+} storage space, leading to less Mg^{2+} intercalation but a stable layer structure.

By Coulomb's law, the electrostatic interaction (u) can be calculated by the following equation:¹⁵²

$$u = \frac{k_e q_1 q_2}{r^2} \quad (1)$$

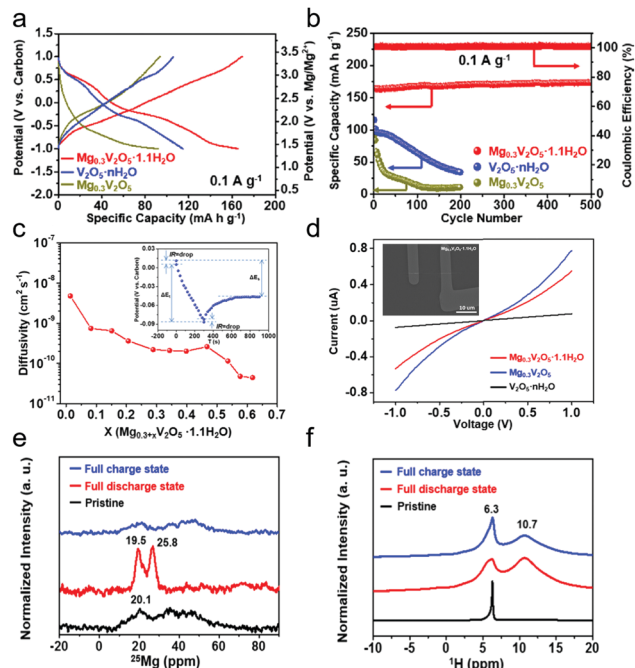


Fig. 19 Charge–discharge curves (a) and cycling performances (b) of $\text{Mg}_{0.3}\text{V}_2\text{O}_5 \cdot 1.1\text{H}_2\text{O}$, $\text{V}_2\text{O}_5 \cdot n\text{H}_2\text{O}$ and $\text{Mg}_{0.3}\text{V}_2\text{O}_5$. (c) Diffusivity of $\text{Mg}_{0.3}\text{V}_2\text{O}_5 \cdot 1.1\text{H}_2\text{O}$ during the discharge process (inset: GITT potential response curve). (d) I - V curves (inset: SEM image of the single $\text{Mg}_{0.3}\text{V}_2\text{O}_5 \cdot 1.1\text{H}_2\text{O}$ nanowire device). ^{25}Mg (e) and ^1H (f) NMR spectra of $\text{Mg}_{0.3}\text{V}_2\text{O}_5 \cdot 1.1\text{H}_2\text{O}$ in the pristine, and fully discharged and charged states. Reproduced from ref. 153, with permission from Cell Press.

where r is the distance between charges, k_e is Coulomb's constant ($k_e \approx 9.0 \times 10^9 \text{ N m}^2 \text{ C}^{-2}$), and q is the charge quantity of the metal ion. It was found that a bivalent alkali earth metal ion possesses stronger electrostatic interactions with host anions. In order to simultaneously acquire large layer spacing, fast ion diffusion and a stable layer structure, Xu *et al.* chose the hydrous bilayered V_2O_5 as the host material, and used a few pre-intercalated Mg^{2+} as pillared ions.¹⁵³ The Mg^{2+} -inserted bilayered V_2O_5 ($\text{Mg}_{0.3}\text{V}_2\text{O}_5 \cdot 1.1\text{H}_2\text{O}$) possesses a reduced interlayer distance of 11.9 Å compared to that of bilayered V_2O_5 . Nevertheless, $\text{Mg}_{0.3}\text{V}_2\text{O}_5 \cdot 1.1\text{H}_2\text{O}$ exhibited a higher capacity and excellent cycling stability compared to that of bilayered V_2O_5 and anhydrous $\text{Mg}_{0.3}\text{V}_2\text{O}_5$ (Fig. 19a and b), which demonstrated that slight Mg^{2+} pre-intercalation not only stabilized the expanded layered structure by strong electrostatic interaction, but also increased the Mg storage activity. The shielding effect of interlayer H_2O was not influenced by the pre-intercalated Mg^{2+} , and the average diffusivity of hydrated Mg^{2+} in $\text{Mg}_{0.3}\text{V}_2\text{O}_5 \cdot 1.1\text{H}_2\text{O}$ was close to that in bilayered V_2O_5 (Fig. 19c). Interestingly, the pre-intercalated Mg^{2+} also enhanced the electron conductivity of the host materials (Fig. 19d). Moreover, the Mg and H nuclear magnetic resonance (NMR) spectra of the pristine, and fully discharged and charged states demonstrated that the pre-intercalated Mg^{2+} and lattice H_2O molecules stably exist in the interlayer of bilayered V_2O_5 during the charge/discharge processes (Fig. 19e and f). Thus, the $\text{Mg}_{0.3}\text{V}_2\text{O}_5 \cdot 1.1\text{H}_2\text{O}$ cathode material is compatible with the

Mg metal anode, but a compatible electrolyte with oxidation stability over 3.5 V and with high Mg deposition/dissolution efficiency has not been obtained and used in this system. Importantly, the synergistic effect of Mg^{2+} and H_2O molecule pre-intercalation endows an ultrastable and fast Mg^{2+} intercalation/de-intercalation, which gives significant inspiration for the future interlayer design of 2D RMB cathodes. Multivalent transition metal ions can also be used to further stabilize the layer structure and enlarge the interlayer distance, resulting from their stronger polarization and larger ionic radius.¹⁵⁴ But this will slightly reduce the specific capacity of the host materials due to the bigger molar mass than that of alkali metal and alkali earth metal ions.

In summary, interlayer regulation has experienced adequate development in RMB cathode materials. It endows fast Mg^{2+} migration kinetics and additionally increased the number of storage sites and structure stability for various layered materials. However, for practical application, the introduced pillar units and the largely expanded interlayer spacing are going to partly reduce the mass and volume energy densities. Generally, when the interlayer distance is greater than 10 Å, the diffusion energy barrier of Mg^{2+} in the interlayer is able to be significantly reduced, according to DFT calculations. Therefore, reasonably controlling the insertion content of pillar units to gain an optimal performance of both high energy density and power density is of great concern in future.

5. Vacancy introduction

Vacancy introduction is a new star in the crystal engineering of cathode materials for RMBs, and it has been identified as an efficient optimization strategy for magnesium storage performance in recent years. The intentionally introduced vacancies would facilitate the diffusion of Mg ions and act as possible intercalation sites in some cases.^{155,156} Thus, introducing vacancies holds promise in enhancing the rate capability and electrochemical activity of cathode materials for RMBs.

The positive effects of cationic vacancy on magnesium storage performance have been demonstrated in anatase TiO_2 . In anatase TiO_2 with monovalent anionic doping (F^- , OH^- , denoted as F-TiO_2) reported by Koketsu *et al.*, a large amount of charge-compensating titanium vacancies were formed.¹⁵⁵ DFT was utilized to calculate the intercalation energies of Mg^{2+} at different sites. The calculated intercalation energies indicate that magnesium ions intercalate more readily into both single- and double-titanium vacancy sites compared to the interstitial site from a thermodynamic perspective (Fig. 20a). Consequently, F-TiO_2 with cation vacancies displayed greatly increased reversible magnesium storage capacity compared to the stoichiometric case (155 vs. 25 mA h g^{-1}) in 0.2 M 2PhMgCl- AlCl_3 /THF electrolyte (Fig. 20b). In addition, F-TiO_2 also delivered superior rate performance and cycling stability in that a capacity of 65 mA h g^{-1} was retained after 500 cycles at 300 mA g^{-1} . Besides, the PDF and magic angle spinning NMR (MAS-NMR) spectroscopy were employed to probe the intercalation sites of magnesium ions in F-TiO_2 . The PDF

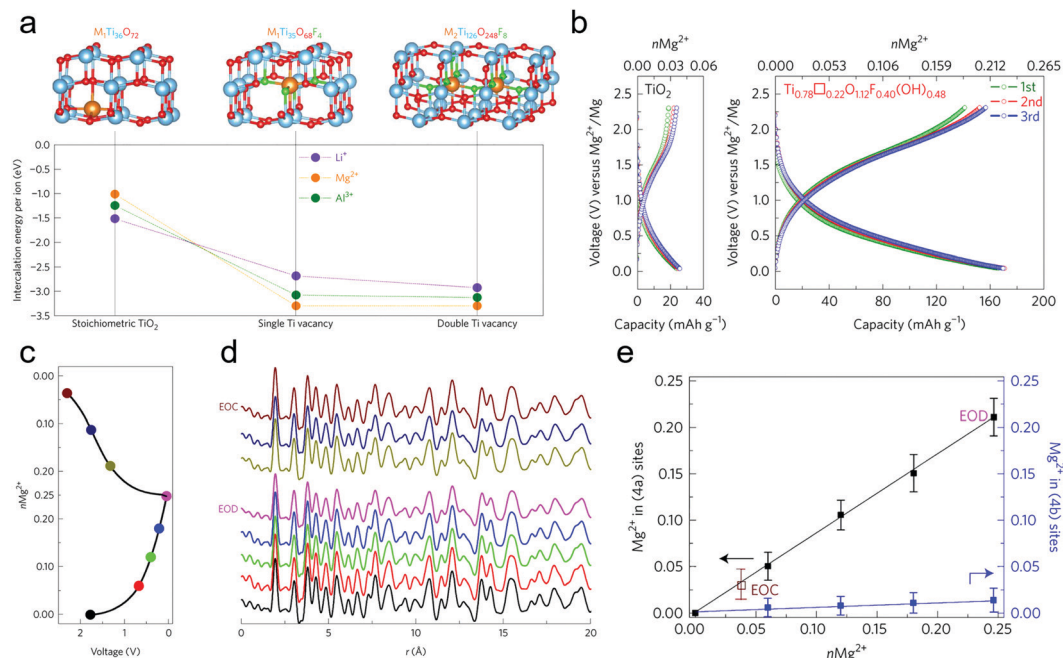


Fig. 20 (a) The structural models and the corresponding intercalation energies for Li, Mg, and Al of defect-free, single-vacancy and double-vacancy anatase. (b) The magnesium storage performance of anatase TiO_2 and cation-deficient anatase TiO_2 . (c) Discharge/charge curves and (d) *ex situ* PDF results of cation-deficient anatase TiO_2 . (e) The occupancy of magnesium ions within the titanium vacancy (4a sites) and octahedral interstices (4b sites). Reproduced from ref. 155, with permission from Nature Publishing Group.

of F- TiO_2 in different charge/discharge states (Fig. 20c and d) and the ^{19}F MAS-NMR spectrum of chemically magnesiated F- TiO_2 confirmed the presence of intercalated magnesium ions mainly in titanium vacancies and fewer in octahedral interstitial sites (Fig. 20e). Moreover, the Mg diffusion coefficients obtained from the GITT show that F- TiO_2 delivers higher diffusion kinetics than TiO_2 . In summary, the Ti vacancies in anatase TiO_2 acted as intercalation sites and facilitated Mg-ion diffusion, thus enhancing the reversible capacity and rate performance.

Besides, anionic vacancy has also been employed to improve the magnesium storage performance. Wang *et al.* fabricated oxygen vacancy-rich black TiO_{2-x} (B- TiO_{2-x}) and evaluated its electrochemical performance as a cathode material for RBMs.¹⁵⁶ The formation of oxygen vacancies was accompanied by the partial reduction of Ti^{4+} to Ti^{3+} , which narrows the band gap and increases the electrical conductivity. B- TiO_{2-x} exhibited enhanced rate performance, *i.e.*, a capacity of 106 mA h g^{-1} at 300 mA g^{-1} , which is about twice that of TiO_2 with few oxygen vacancies.

These two representative works demonstrate the possibility of improving magnesium storage performance *via* vacancy introduction. The positive effects of both cationic and anionic vacancies on magnesium storage were verified in the example parent material TiO_2 , but the extension to other promising cathode materials for RBMs is still almost non-existent and has a long way to go. On the other hand, many high-capacity cathode materials for RBMs suffer from poor cycling stability, and it is not clear whether vacancies can play a positive role in improving cycling stability. This is indefinite, but at least no

negative effects on cycling stability were observed in vacancy-rich TiO_2 .

6. Amorphization

Owing to the strong interaction between magnesium ions and hosts, especially oxides, the structural integrity of cathode materials is difficult to maintain during the repeated intercalation/deintercalation of magnesium ions, resulting in capacity decay. The loose frameworks of amorphous materials hold promise to accommodate the volume change originating from magnesium-ion intercalation and thus to maintain the structural integrity and achieve better reversibility.^{157,158} On the other hand, the structural defects, such as vacancies and void spaces, in amorphous materials may be able to act as ion storage sites, which would increase the capacity.¹⁵⁹ Therefore, amorphization is a promising strategy to fabricate high-capacity and long-life cathode materials for RBMs.

Some researchers have attempted to exploit amorphous cathode materials for RBMs. For example, Arthur *et al.* fabricated V_2O_5 -based amorphous powders by ball-milling with the addition of P_2O_5 and investigated their magnesium storage performance.¹⁵⁷ In contrast to the low magnesium storage activity of polycrystalline V_2O_5 , the amorphous $\text{V}_2\text{O}_5\text{-P}_2\text{O}_5$ (75:25) cathode material displayed largely enhanced magnesium storage capacity (121 mA h g^{-1}). In addition, the crystallization products from amorphous $\text{V}_2\text{O}_5\text{-P}_2\text{O}_5$ displayed degraded electrochemical performance, further demonstrating the superiority of the amorphous structure for magnesium

storage in this system. Besides, amorphous FePO_4 reported by Mathew *et al.* also delivers attractive magnesium storage capacity.¹⁵⁸ However, both these works employ $\text{Mg}(\text{ClO}_4)_2/\text{CH}_3\text{CN}$ electrolyte, which is incompatible with the Mg anode because of the passivation effect. Considering practical application, the use of an electrolyte possessing good compatibility with both Mg anode and cathode materials is a key point.

Furthermore, amorphization can be combined with nanostructure construction to further improve the Mg storage performance of cathode materials. Cheng *et al.* investigated the magnesium storage performance of vanadium oxide nanoclusters with an amorphous nature (Fig. 21a) in $[\text{Mg}_2(\mu\text{-Cl})_2(\text{DME})_4][\text{AlCl}_4]_2/\text{DME}$ electrolyte.¹⁶⁰ The V_2O_5 nanoclusters/porous carbon ($\text{V}_2\text{O}_5/\text{RFC}$) composite delivers a high capacity of over 200 mA h g^{-1} at 40 mA g^{-1} in the range of 0.5–2.8 V (vs. Mg^{2+}/Mg) (Fig. 21b). At 640 mA g^{-1} , a capacity of about 100 mA h g^{-1} was still obtained. Unfortunately, the expected cycling stability of amorphous materials is absent in this composite. During the cycling process, the capacity of $\text{V}_2\text{O}_5/\text{RFC}$ decays fast in the first several cycles, especially at low current density (Fig. 21c and d). The capacity fading may be attributed to the detachment of V_2O_5 nanoclusters from the porous carbon substrate during the repeated magnesiation/demagnesiation process rather than the destruction of the amorphous structure. In addition, amorphous MoS_x nanoclusters also display potential as cathode materials for RMBs.¹⁶¹

Although the enhanced magnesium storage activity of some amorphous cathode materials for RMBs has been reported, the related investigations are still rare. The extension of amorphization to other cathode materials is worth exploring. Further optimizing the structure to sufficiently utilize the advantage of amorphization is important for attaining high-performance

amorphous cathode materials. In addition, the actual effects of amorphization on magnesium storage performance are still unidentified, and more effort is required.

7. The development of unique crystal frameworks

In addition to regulating the main crystal frameworks for obtaining better electrochemical performance, designing or developing cathode materials with new, unique crystal structures is also significantly important to promote the development of high-energy RMBs. This is considered as a kind of crystal engineering to meet the demands of Mg^{2+} and other multivalent ion intercalation chemistries.

7.1. 3D open framework

A system containing voids with sizes ranging from a few angstroms to hundreds of angstroms is usually considered as a 3D open framework.^{162,163} Its open channels with large sizes are conducive to facilitating the migration and storage of Mg^{2+} . Jacobson *et al.* designed a 3D microporous $\text{Mo}_{2.5+y}\text{VO}_{9+\delta}$ ($\text{Mo}_{2.48}\text{VO}_{9.93}$) material originally for Li^+ ion storage.¹⁶⁴ Subsequently, its large microporous structure and rich redox valances from $\text{Mo}^{5+/6+}$ and $\text{V}^{4+/5+}$ endowed it with great potential for Mg^{2+} intercalation.¹⁶⁵ In $\text{Mo}_{2.5+y}\text{VO}_{9+\delta}$, the three-, six-, and seven-membered ring-type tunnels are enclosed by corner-sharing MO_6 octahedra and pentagonal $[(\text{Mo})\text{Mo}_5\text{O}_{27}]$ units formed by a MoO_7 pentagonal bipyramid and five edge-sharing MoO_6 octahedra (Fig. 22a). Apart from the advantages of open and stable ion tunnels, the oxygen lattice bound by

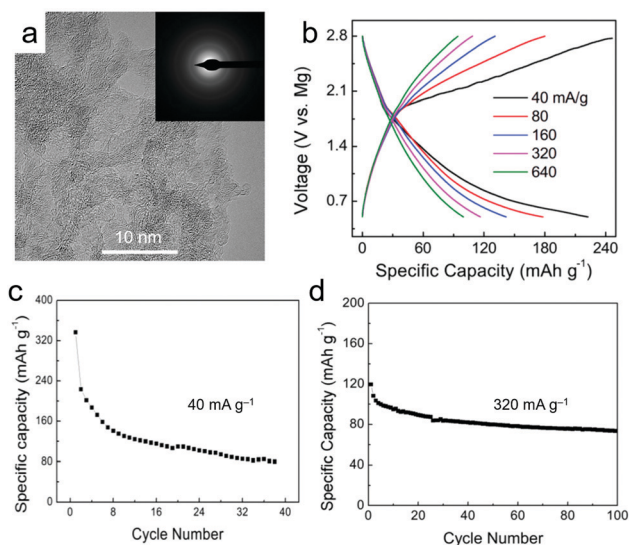


Fig. 21 (a) HRTEM image and SAED pattern (inset) of the amorphous $\text{V}_2\text{O}_5/\text{RFC}$ composite; (b) the charge/discharge curves at different current densities and (c and d) the cycling performance at 40 and 320 mA g^{-1} of the amorphous $\text{V}_2\text{O}_5/\text{RFC}$ composite. Reproduced from ref. 160, with permission from Wiley-VCH.

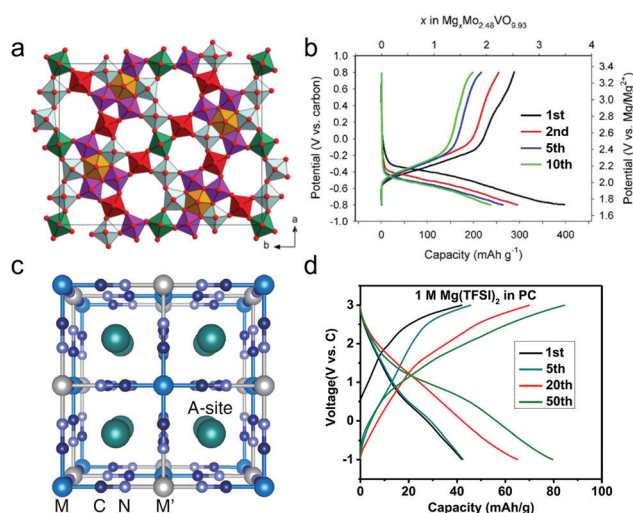


Fig. 22 (a) Crystal structure of $\text{Mo}_{2.5+y}\text{VO}_{9+\delta}$ (green, $\text{Mo}^{5+}/\text{V}^{4+}$; red, $\text{Mo}^{6+}/\text{V}^{5+}$; blue, $\text{Mo}^{6+}/\text{Mo}^{5+}$; orange, Mo^{5+} ; and purple, Mo^{6+}). (b) Discharge-charge curves of an $\text{AC}/\text{Mo}_{2.48}\text{VO}_{9.93}$ cell at 2 mA g^{-1} . Reproduced from ref. 165, with permission from the American Chemical Society. (c) Structure of the PBA $\text{A}_x\text{MIM}(\text{CN})_6]_{1-y} \cdot n\text{H}_2\text{O}$. Reproduced from ref. 169, with permission from IOP Publishing. (d) Discharge-charge curves of NiFe-PBAs at 10 mA g^{-1} . Reproduced from ref. 173, with permission from Elsevier.

high oxidation state metal ions facilitates achieving local electroneutrality and lower Mg^{2+} diffusion barriers.¹⁶⁶ When evaluated as a RMB cathode, it could display a high discharge capacity of 397 mA h g^{-1} (3.49 Mg^{2+} per formula) with short plateaus of 2.15 and 1.75 V vs. Mg^{2+}/Mg at the first cycle in $\text{Mg}(\text{TFSI})_2/\text{AN}$ (Fig. 22b). This suggests that a promising energy density of approximately 790 W h kg^{-1} may be obtained. Upon Mg^{2+} intercalation, a single-phase solid solution reaction was demonstrated by *ex situ* XRD, while the intercalation is highly reversible.

Prussian blue (PB) and its analogues (PBAs) are typically open frameworks. They have received great attention from researchers as potential cathode materials for LIBs, SIBs and other multivalence ion batteries.^{167,168} The general formula of PBAs is $\text{A}_x\text{M}[\text{M}'(\text{CN})_6]_{1-y}\cdot n\text{H}_2\text{O}$, where M and M' are transition-metal ions octahedrally coordinated with six triple-bonded CN ligands respectively, forming microporous frameworks with open and large spaces (Fig. 22c); A as the carrier ions and H_2O molecules occupy the large open cages (A-site, $\sim 4.6 \text{ \AA}$ in diameter).¹⁶⁹ The y value is the fraction of the primary M or M'-site vacancies. Some CuFe-PBAs,^{169,170} NiFe-PBAs,^{171–174} FeFe-PBAs,¹⁷⁵ and sodium/potassium-containing PBAs^{176,177} have been investigated in aqueous and organic RMBs, and hybrid Mg-ion systems. They usually delivered stable capacities of $50\text{--}70 \text{ mA h g}^{-1}$ with a plateau of approximately 3.0 V vs Mg^{2+}/Mg contributed by the main $\text{Fe}^{3+}/\text{Fe}^{2+}$ redox (Fig. 22d).¹⁷³ The cubic CuFe-PBAs, NiFe-PBAs and ZnFe-PBAs mainly exhibited a single-phase Mg^{2+} insertion/extraction mechanism. Based on the stable framework and the broad ion diffusion channels, superior cycling and rate performances could be obtained. One of the key factors to deliver capacity is the solvent molecule structure of the electrolyte that determines the configuration and desolvation energy of the solvated Mg^{2+} ion.¹⁶⁹ In aqueous electrolyte, the high desolvation energy of $\text{Mg}(\text{H}_2\text{O})_6^{2+}$ leads to a co-intercalation mechanism, which also facilitates a faster diffusion kinetics. In organic electrolytes using long-chain ethers as solvents, such as triglyme, TEGDME and so forth, complete desolvation is necessary for Mg^{2+} intercalation because of the oversized length. For the short-chain molecule solvated Mg^{2+} ions, the co-intercalation reaction in PBAs is also probable. Besides, the defects and crystal water contents have important influences on the specific capacity and cycling stability of PBAs during the Mg^{2+} intercalation process, but the related research is rarely reported.

7.2. 1D atomic-chain structure

Recently, some chain-like transition metal polysulfides, such as VS_4 ,^{178–182} TiS_3 ,¹⁸³ NbS_3 ,¹⁸⁴ and so forth, have received much attention for multivalence ion intercalation. The atomic-chains are loosely stacked by weak van der Waals forces. The weak interactions between neighboring atomic chains favorably facilitate the Mg^{2+} migration kinetics. Moreover, compared to 2D layered materials, the 1D chain-like structures possess more open ion migration channels. VS_4 is a typical “linear-chain” compound, and its interchain distance is 5.83 \AA (Fig. 23a), which is comparable to the interlayer distance of the layered VS_2 (5.8 \AA). Wang *et al.* firstly employed VS_4 nanorods as a RMB

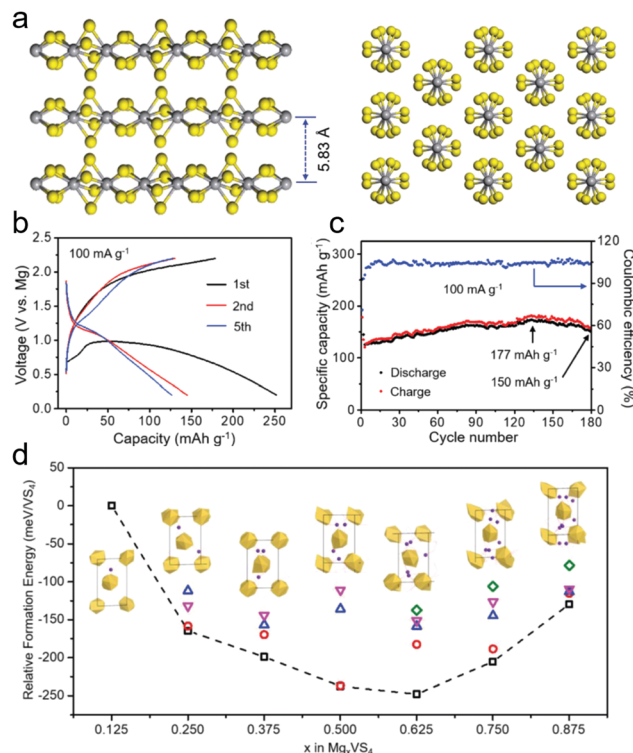


Fig. 23 (a) Crystal structure of the atom-chain VS_4 . Discharge–charge curves (b) and cycling performance (c) of VS_4 nanorods at 100 mA g^{-1} in APC electrolyte. (d) DFT-calculated formation energy of Mg_xVS_4 supercells at different contents of Mg^{2+} occupation. Reproduced from ref. 178, with permission from Wiley-VCH.

cathode material.¹⁷⁸ When discharged to 0.2 V in APC electrolyte, the VS_4 nanorods exhibited an initial discharge capacity of 251 mA h g^{-1} (0.84 Mg^{2+} per formula) at 100 mA g^{-1} (Fig. 23b). Due to the partially irreversible extraction of Mg^{2+} in the initial charge, a reversible charge capacity of 179 mA h g^{-1} was obtained (Fig. 23c). Then a stable specific capacity of approximately 150 mA h g^{-1} could be maintained until the 180th cycle. Interestingly, the Mg^{2+} storage mechanism in VS_4 is different from the conversion reaction of VS_4 during sodiation.¹⁸⁵ The *ex situ* XRD and Raman results indicated that the intercalation/extraction of Mg^{2+} has a very slight influence on the stability of the V–S chain of VS_4 , demonstrating a single-phase reaction mechanism. To further verify this mechanism, DFT calculations were used to obtain the average relative formation energy of Mg_xVS_4 with the Mg content ranging from 0.125 to 0.875 (Fig. 23d). From 0.125 to 0.625, the intercalation of Mg^{2+} was increasingly energetically favorable. Although the formation energy gradually increased upon subsequent Mg^{2+} insertion, intercalation of Mg^{2+} was still energetically favorable. These results demonstrated that the intercalation of Mg^{2+} in VS_4 is a single-phase process and is thermodynamically favorable. Our group further expanded chain-like $\text{VS}_4@r\text{GO}$ by pre-intercalation of PY_{14}^+ , and thereby obtained a higher capacity of $268.3 \text{ mA h g}^{-1}$, a remarkable rate performance of 85.9 mA h g^{-1} at 2 A g^{-1} and outstanding temperature adaptability (-35 to $55 \text{ }^\circ\text{C}$).¹⁷⁹

The exploitation of new frameworks with an active redox center still faces many challenges in crystallography and synthetics. The typical open frameworks reported in other fields, such as zeolite-like materials, metal-organic frameworks (MOFs) and covalent organic frameworks (COFs), may exhibit unique properties for Mg^{2+} intercalation chemistry in the future.

8. Conclusions and outlook

In conclusion, we summarized the current crystal regulation strategies for modifying the various Chevrel, spinel, layered, olivine materials and so forth, while discussing their advantages/drawbacks and some ambiguous controversies. Topochemical substitution can facilitate to obtain insertion-type RMB cathode materials, which is significant to develop new crystal frameworks for reversible Mg^{2+} storage and diffusion. Substitution doping and vacancy introduction can subtly control the energy band, the localized electron configuration of crystals and Mg migration channels, further facilitating the kinetics and magnesiation concentration. Interlayer regulation of promising layered materials effectively decreases the Mg migration energy barriers, and increases the Mg storage sites and structural stability. Amorphization is able to liberate the Mg storage capacity at the expense of the stable voltage platform. Benefiting from these strategies, the electrochemical performances of many RMB cathode materials have been largely improved. Besides, some unique frameworks accommodating fast and stable Mg^{2+} intercalation, including binary Mo-V oxides, Prussian blue analogues and atom-chain polysulfides, were also introduced. The specific capacities, working voltages and the corresponding energy densities and power densities of the representative modified materials were further included, as shown in Fig. 24 and Table 1. The modified spinel $\lambda\text{-MnO}_2$, olivine materials, bilayered V_2O_5 , layered MnO_2 and $\text{Mo}_{2.48}\text{VO}_{9.93}$ exhibit significant prospects by virtue of their high energy densities over 500 Wh kg^{-1} and high voltages of more than $2.0 \text{ V vs. Mg}^{2+}/\text{Mg}$ (Fig. 24a). Meanwhile, the average diffusion coefficient of Mg^{2+} as a key parameter was improved to the order of magnitude of $10^{-10} \text{ cm}^2 \text{ s}^{-1}$ in $\text{Mg}^{2+}/\text{H}_2\text{O}$ -inserted bilayered V_2O_5 and similar layered materials, benefiting from the shielding effect or solvent co-intercalation. The diffusion coefficient is similar to that of Li^+ in LiFePO_4 . Therefore, they exhibit high power densities over 5 kW kg^{-1} (Fig. 24b). Unfortunately, these outstanding electrochemical performances are mostly obtained in the systems consisting of aqueous or organic electrolytes that cannot dissolve/deposit Mg metal and AC counter electrodes. This suggested that there are very few compatible electrolytes for achieving the full performance of these promising cathode materials with Mg metal over $2 \text{ V vs. Mg}^{2+}/\text{Mg}$, although many high-efficiency electrolytes with oxidation stability over 3.5 V have been developed. Therefore, the development of commercial high-energy RMBs still remains very difficult.

According to the above-mentioned discussions, the compatibility mechanism between high-voltage cathode materials and highly anodically stable electrolytes is very important but lacks

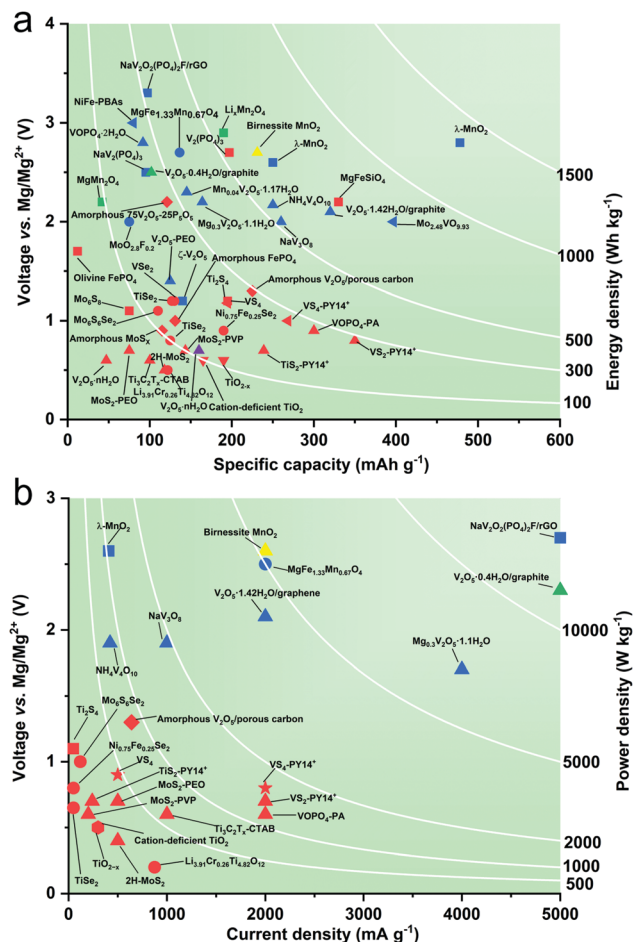


Fig. 24 Energy densities (a) and power densities (b) of representative RMB cathode materials after crystal modification. The square, circle, triangle, hexagon, rhombus and star symbols correspond to topochemical substitution, substitution doping, interlayer regulation, vacancy introduction, amorphization and unique crystal frameworks, respectively; red, blue, green, purple, and yellow represent different counter electrodes, *i.e.* Mg metal, active carbon (AC), Pt, Sn, and MnO_2 , respectively.

investigations. The high energy penalty for breaking Mg-Cl bonds in chlorinated electrolytes and the high desolvation energy in halogen-free electrolytes at the cathode/electrolyte interface may dramatically decrease the Mg ion intercalation kinetics, leading to low capacity, especially in close-packed frameworks. In these cases, SEI design or surface modification by crystal regulation, and electrolyte optimization are critical to achieve good compatibility between cathode and electrolyte.

From the aspect of cathode materials, crystal regulation, especially multi-atomic substitution doping (cation and anion) and vacancy introduction, still needs to be largely developed to improve the electrochemical performance of the promising materials, such as high-voltage NAISCON, olivine silicates, fluorophosphates and so forth. For the interlayer regulation, the insertion content of pillar units in the layered oxides should be well controlled for the optimal mass and volume energy densities. The co-intercalation of Mg^{2+} and solvent is an effective strategy, but puts forward higher demands on the structural

Table 1 Summary of representative RMB cathode materials after crystal modification

Crystal regulation	Cathode materials	Highest specific capacity/current density (mA h g ⁻¹ /mA g ⁻¹)	Average discharge potential (V, vs. Mg ²⁺ /Mg)	Rate performance (mA h g ⁻¹ /mA g ⁻¹)	Cycling performance (mA h g ⁻¹ /mA g ⁻¹)	Electrolyte	Counter electrode	Ref.
TS	Chevreil Mo ₆ S ₈	~75/—	~1.1	—	—/>>2000/—	0.25 M Mg(AlCl ₂ Et) ₂ /THF	Mg	23
TS	λ-MnO ₂	250/—	~2.6	—	70/38/—	0.2 M Mg(TFSI) ₂ /PC	AC	52
TS	λ-MnO ₂	478.4/13.6	~2.8	253.9/408	155.6/300/136	1 M MgCl ₂ /H ₂ O	Graphite	49
TS	Spinel Li _x Mn ₂ O ₄ (x ≈ 0.2)	190/13.5	~2.9	—	—	1 M Mg(NO ₃) ₂ /H ₂ O	Pt	50
TS	Spinel MgMn ₂ O ₄	42/45.5	~2.2	—	42/20/45.5	1 M Mg(NO ₃) ₂ /H ₂ O	Pt	48
TS	Spinel Ti ₂ S ₄	195/12	~1.2	175/48	140/40/24	2PhMgCl-AlCl ₃ /tetraglyme	Mg	58
TS	V ₂ (PO ₄) ₃	197/10	~2.7	—	197/5/10	0.5 M Mg(TFSI) ₂ /AN	Mg	68
TS	NaV ₂ (PO ₄) ₃	95.3/20	~2.5	—	77.2/100/20	0.3 M Mg(TFSI) ₂ /AN	AC	69
TS	MgFesSiO ₄	330/6.62	~2.2	—	33.0/5/6.62	0.5 M Mg(TFSI) ₂ /AN	Mg	87
TS	Olivine FePO ₄	12/2.5	~1.7	—	6/20/2.5	0.3 M Mg(CB ₁₁ H ₁₂) ₂ /tetraglyme	Mg	85
TS	ζ-V ₂ O ₅	140/6	~1.2	—	90/100/6	0.2 M Mg(TFSI) ₂ /PC	AC	92
TS	NaV ₂ O ₂ (PO ₄) ₂ F/rGO	97.2/20	~3.3	30.3/5000	81/1000/100	0.3 M Mg(TFSI) ₂ /AN	AC	98
SD	Ni _{0.75} Fe _{0.25} Se ₂	190/10	~0.9	120/50	45.6/9500/500	0.25 M 2PhMgCl-AlCl ₃ /THF	Mg	100
SD	Li _{3.91} Cr _{0.26} Ti _{14.82} O ₁₂	122/17.5	~0.5	30/875	148/500/20	0.05 M MgF ₂ + 0.5 M THFPB in DME	Mg	102
SD	MgFe _{1.33} Mn _{0.67} O ₄	136.5/50	~2.7	80/2000	76/150/87.5	0.5 M MgCl ₂ /H ₂ O	AC	104
SD	Mo ₆ S ₆ Se ₂	~110/15	~1.1	~80/120	88.3/1000/1000	0.25 M Mg(AlCl ₂ Et) ₂ /THF	Mg	109
SD	TiSe ₂	~125/5	~0.8	~63/50	~100/100/15	0.25 M Mg(AlCl ₂ Et) ₂ /THF	Mg	108
SD	TiSe ₂	127/5	~1.2	—	80/40/5	2PhMgCl-AlCl ₃ /THF	Mg	106
SD	VSe ₂	~130/5	~1.2	—	86/40/5	2PhMgCl-AlCl ₃ /THF	Mg	106
SD	MoO _{2.8} F _{0.2}	~75/—	~2.0	—	~70/18/—	0.2 M Mg(TFSI) ₂ /PC	Carbon black	111
IR	V ₂ O ₅ ·nH ₂ O	160/20	~0.7 (against Sn anode)	—	~120/50/30	1 M Mg(ClO ₄) ₂ /AN	Sn	117
IR	V ₂ O ₅ ·0.4H ₂ O/graphite	102/1000	~2.1	44/5000	80/10/1000	Mg(NO ₃) ₂ /H ₂ O	Pt	134
IR	V ₂ O ₅ ·1.42H ₂ O/graphene	320/50	~2.5	100/2000	~100/500/1000	0.5 M Mg(TFSI) ₂ /AN	AC	138
IR	V ₂ O ₅ ·nH ₂ O	47/20 (μA cm ⁻²)	~0.6	—	47/10/20 (μA cm ⁻²)	1.0 M Mg(TFSI) ₂ /diglyme	Mg	119
IR	Birnessite MnO ₂	231.1/100	~2.7	112/2000	55/10000/2000	0.5 M Mg(ClO ₄) ₂ /H ₂ O	Birnessite	118
IR	VOPO ₄ ·2H ₂ O	91.7/5	~2.8	—	~95/50/5	0.1 M Mg(ClO ₄) ₂ ·6H ₂ O/PC	MnO ₂	120
IR	NaV ₃ O ₈	260/50	~2.0	62.4/1000	~160/100/100	0.5 M Mg(ClO ₄) ₂ /AN	Carbon	151
IR	Mg _{0.3} V ₂ O ₅ ·1.1H ₂ O	164/100	~2.2	50/4000	~90/10000/2000	0.3 M Mg(TFSI) ₂ /AN	AC	153
IR	Mn _{0.04} V ₂ O ₅ ·1.17H ₂ O	145/50	~2.3	50/4000	~80/10000/2000	0.3 M Mg(TFSI) ₂ /AN	AC	154
IR	MoS ₂ -PEO	75/5	~0.7	~20/500	~70/100/5	0.25 M 2PhMgCl-AlCl ₃ /THF	Mg	140
IR	MoS ₂ -PVP	143.4/20	~0.7	43/200	13.2/100/20	0.25 M 2PhMgCl-AlCl ₃ /THF	Mg	142
IR	V ₂ O ₅ -PEO	125/10	~1.4	—	96/35/10	0.5 M Mg(ClO ₄) ₂ /AN	Carbon	141
IR	TiS ₂ -PY14 ⁺	239/24	~0.7	179/240	~115/500/240	0.25 M 2PhMgCl-AlCl ₃ /THF with 0.2 M PY14Cl	Mg	144
IR	VS ₂ -PY14 ⁺	~350/20	~0.8	214/2000	200/300/1000	0.4 M 2PhMgCl-AlCl ₃ /THF with 0.2 M PY14Cl	Mg	146
IR	Ti ₃ C ₂ T _x -CTAB	100/50	~0.6	42/1000	45/250/200	0.4 M 2PhMgCl-AlCl ₃ /THF	Mg	145
IR	VOPO ₄ -PA	~300/50	~0.9	109/2000	192/500/100	0.25 M 2PhMgCl-AlCl ₃ /THF	Mg	143
IR	NH ₄ V ₄ O ₁₀	~250/42.1	~2.17	68.9/421.2	36.8/100/210.6	0.5 M Mg(ClO ₄) ₂ /AN	AC	121
IR	2H-MoS ₂	118/10	~0.5	~50/500	56/200/100	0.4 M MgBQ/DME	Mg	115
VI	Cation-deficient TiO ₂	165/20	~0.6	~75/300	65/500/300	0.2 M 2PhMgCl-AlCl ₃ /THF	Mg	155
VI	TiO _{2-x}	190/50	~0.6	106/300	77/400/300	0.4 M 2PhMgCl-AlCl ₃ /THF	Mg	156
A	Amorphous 75V ₂ O ₅ -25P ₂ O ₅	121/5	~2.2	—	57/5/5	1 M Mg(ClO ₄) ₂ /AN	Mg	157

Table 1 (continued)

Crystal regulation	Cathode materials	Highest specific capacity/current density (mA h g ⁻¹ /mA g ⁻¹)	Average discharge potential (V, vs. Mg ²⁺ /Mg)	Rate performance (mA h g ⁻¹ /mA g ⁻¹)	Cycling performance (mA h g ⁻¹ /h/mA g ⁻¹)	Electrolyte	Counter electrode	Ref.
A	Amorphous FePO ₄	131/5	~1.0	—	—	1 M Mg(ClO ₄) ₂ /AN	Mg	158
A	Amorphous V ₂ O ₅ /porous carbon	~225/40	~1.3	~100/640	~76/100/320	0.2 M [Mg ₂ (μ-Cl) ₂ (DME) ₄][AlCl ₄] ₂ /DME,	Mg	160
A	Amorphous MoS _x	115/10	~0.9	—	75/3/10	0.25 M Mg(AlCl ₂ BuEt) ₂ /THF	Mg	161
UCF	Mo _{2.48} VO _{9.93}	397/2	~2.0	—	235/15/2	0.5 M Mg(TFSI) ₂ /AN	AC	165
UCF	NiFe-PBAS	80/10	~3.0	—	40/50/10	1 M Mg(TFSI) ₂ /PC	AC	173
UCF	VS ₄	195/100	~1.18	106/500	74/800/500	0.4 M 2PhMgCl-AlCl ₃ /THF	Mg	178
UCF	VS ₄ -PY14 ⁺	268.3/50	~1.0	85.9/2000	78.9/200/500	0.25 M 2PhMgCl-AlCl ₃ /THF with 0.2 M PY14Cl	Mg	179

Topochemical substitution: TS; substitution doping: SD; interlayer regulation: IR; vacancy introduction: VI; amorphization: A and the unique crystal frameworks: UCFs.

stability and site space of the crystal framework for the repeated insertion/extraction of the large solvated ion. Moreover, crystal engineering that builds more open frameworks from molecule or atom to crystal for faster Mg²⁺ migration and storage, such as MOFs, 2D van der Waals heterostructures, and COFs, may receive much attention in the future. This aims at developing cathodes with discharge voltage over 3.0 V vs. Mg²⁺/Mg and an energy density of 600 W h kg⁻¹. The mass loading of cathode materials should also be increased in laboratory research for better access to practical application. Finally, we hope that this review will provide a significant reference and enlightenment for the future research on reversible Mg batteries and other multivalence ion batteries.

Conflicts of interest

The authors declare no competing financial interests.

Acknowledgements

This work was supported by the National Natural Science Fund for Distinguished Young Scholars (51425204), the National Natural Science Foundation of China (51521001, 51972259, 51602239), the National Key Research and Development Program of China (2016YFA0202603), the Programme of Introducing Talents of Discipline to Universities (B17034), and the Yellow Crane Talent (Science & Technology) Program of Wuhan City.

Notes and references

- B. Dunn, H. Kamath and J.-M. Tarascon, *Science*, 2011, **334**, 928–935.
- J. B. Goodenough and K.-S. Park, *J. Am. Chem. Soc.*, 2013, **135**, 1167–1176.
- J.-M. Tarascon and M. Armand, *Nature*, 2001, **414**, 359.
- V. Etacheri, R. Marom, R. Elazari, G. Salitra and D. Aurbach, *Energy Environ. Sci.*, 2011, **4**, 3243–3262.
- M. S. Whittingham, *Chem. Rev.*, 2014, **114**, 11414–11443.
- D. Lin, Y. Liu and Y. Cui, *Nat. Nanotechnol.*, 2017, **12**, 194.
- S. Ni, S. Tan, Q. An and L. Mai, *J. Energy Chem.*, 2020, **44**, 73–89.
- R. Zhang, N. W. Li, X. B. Cheng, Y. X. Yin, Q. Zhang and Y. G. Guo, *Adv. Sci.*, 2017, **4**, 1600445.
- X.-B. Cheng, R. Zhang, C.-Z. Zhao and Q. Zhang, *Chem. Rev.*, 2017, **117**, 10403–10473.
- C. Niu, H. Pan, W. Xu, J. Xiao, J.-G. Zhang, L. Luo, C. Wang, D. Mei, J. Meng and X. Wang, *Nat. Nanotechnol.*, 2019, **14**, 594–601.
- C. Niu, H. Lee, S. Chen, Q. Li, J. Du, W. Xu, J.-G. Zhang, M. S. Whittingham, J. Xiao and J. Liu, *Nat. Energy*, 2019, **4**, 551–559.
- J. W. Choi and D. Aurbach, *Nat. Rev. Mater.*, 2016, **1**, 16013.
- X. Xu, F. Xiong, J. Meng, X. Wang, C. Niu, Q. An and L. Mai, *Adv. Funct. Mater.*, 2020, **30**, 1904398.

- 14 R. C. Massé, E. Uchaker and G. Cao, *Sci. China Mater.*, 2015, **58**, 715–766.
- 15 H. D. Yoo, I. Shterenberg, Y. Gofer, G. Gershinsky, N. Pour and D. Aurbach, *Energy Environ. Sci.*, 2013, **6**, 2265–2279.
- 16 H. Tang, Z. Peng, L. Wu, F. Xiong, C. Pei, Q. An and L. Mai, *Electrochem. Energy Rev.*, 2018, **1**, 169–199.
- 17 P. Canepa, G. Sai Gautam, D. C. Hannah, R. Malik, M. Liu, K. G. Gallagher, K. A. Persson and G. Ceder, *Chem. Rev.*, 2017, **117**, 4287–4341.
- 18 A. Ponrouch, J. Bitenc, R. Dominko, N. Lindahl, P. Johansson and M. R. Palacin, *Energy Storage Mater.*, 2019, **20**, 253–262.
- 19 M. Mao, T. Gao, S. Hou and C. Wang, *Chem. Soc. Rev.*, 2018, **47**, 8804–8841.
- 20 R. Deivanayagam, B. J. Ingram and R. Shahbazian-Yassar, *Energy Storage Mater.*, 2019, **21**, 136–153.
- 21 Z. Li, L. Han, Y. Wang, X. Li, J. Lu and X. Hu, *Small*, 2019, **15**, 1900105.
- 22 J. Song, E. Sahadeo, M. Noked and S. B. Lee, *J. Phys. Chem. Lett.*, 2016, **7**, 1736–1749.
- 23 T. D. Gregory, R. J. Hoffman and R. C. Winterton, *J. Electrochem. Soc.*, 1990, **137**, 775–780.
- 24 D. Aurbach, Z. Lu, A. Schechter, Y. Gofer, H. Gizbar, R. Turgeman, Y. Cohen, M. Moshkovich and E. Levi, *Nature*, 2000, **407**, 724.
- 25 L. Li, Y. Lu, Q. Zhang, S. Zhao, Z. Hu and S. L. Chou, *Small*, 2019, 1902767.
- 26 J. Muldoon, C. B. Bucur and T. Gregory, *Chem. Rev.*, 2014, **114**, 11683–11720.
- 27 I. Shterenberg, M. Salama, Y. Gofer, E. Levi and D. Aurbach, *MRS Bull.*, 2014, **39**, 453–460.
- 28 X. Xiao, H. Wang, P. Urbankowski and Y. Gogotsi, *Chem. Soc. Rev.*, 2018, **47**, 8744–8765.
- 29 K. T. Lee, T. Ramesh, F. Nan, G. Botton and L. F. Nazar, *Chem. Mater.*, 2011, **23**, 3593–3600.
- 30 R. Chevrel, M. Sergent and J. Prigent, *J. Solid State Chem.*, 1971, **3**, 515–519.
- 31 P. Mulhern and R. Haering, *Can. J. Phys.*, 1984, **62**, 527–531.
- 32 M. S. Chae, J. W. Heo, S.-C. Lim and S.-T. Hong, *Inorg. Chem.*, 2016, **55**, 3294–3301.
- 33 Y. Cheng, L. Luo, L. Zhong, J. Chen, B. Li, W. Wang, S. X. Mao, C. Wang, V. L. Sprenkle and G. Li, *ACS Appl. Mater. Interfaces*, 2016, **8**, 13673–13677.
- 34 L. Geng, G. Lv, X. Xing and J. Guo, *Chem. Mater.*, 2015, **27**, 4926–4929.
- 35 E. Levi, G. Gershinsky, D. Aurbach, O. Isnard and G. Ceder, *Chem. Mater.*, 2009, **21**, 1390–1399.
- 36 L. F. Wan, B. R. Perdue, C. A. Apblett and D. Prendergast, *Chem. Mater.*, 2015, **27**, 5932–5940.
- 37 M. Levi, E. Lancry, H. Gizbar, Z. Lu, E. Levi, Y. Gofer and D. Aurbach, *J. Electrochem. Soc.*, 2004, **151**, A1044–A1051.
- 38 E. Levi, E. Lancry, A. Mitelman, D. Aurbach, G. Ceder, D. Morgan and O. Isnard, *Chem. Mater.*, 2006, **18**, 5492–5503.
- 39 M. Levi, E. Lancry, H. Gizbar, Y. Gofer, E. Levi and D. Aurbach, *Electrochim. Acta*, 2004, **49**, 3201–3209.
- 40 M. Thackeray, W. David, P. Bruce and J. B. Goodenough, *Mater. Res. Bull.*, 1983, **18**, 461–472.
- 41 E. Hosono, T. Kudo, I. Honma, H. Matsuda and H. Zhou, *Nano Lett.*, 2009, **9**, 1045–1051.
- 42 D. K. Kim, P. Muralidharan, H.-W. Lee, R. Ruffo, Y. Yang, C. K. Chan, H. Peng, R. A. Huggins and Y. Cui, *Nano Lett.*, 2008, **8**, 3948–3952.
- 43 M. Liu, Z. Rong, R. Malik, P. Canepa, A. Jain, G. Ceder and K. A. Persson, *Energy Environ. Sci.*, 2015, **8**, 964–974.
- 44 J. Lee, D. A. Kitchaev, D.-H. Kwon, C.-W. Lee, J. K. Papp, Y.-S. Liu, Z. Lun, R. J. Clément, T. Shi and B. D. McCloskey, *Nature*, 2018, **556**, 185.
- 45 S. Okamoto, T. Ichitsubo, T. Kawaguchi, Y. Kumagai, F. Oba, S. Yagi, K. Shimokawa, N. Goto, T. Doi and E. Matsubara, *Adv. Sci.*, 2015, **2**, 1500072.
- 46 Q. D. Truong, H. Kobayashi and I. Honma, *RSC Adv.*, 2019, **9**, 36717–36725.
- 47 Q. D. Truong, M. Kempaiah Devaraju, P. D. Tran, Y. Gambe, K. Nayuki, Y. Sasaki and I. Honma, *Chem. Mater.*, 2017, **29**, 6245–6251.
- 48 N. N. Sinha and N. Munichandraiah, *Electrochem. Solid-State Lett.*, 2008, **11**, F23–F26.
- 49 C. Yuan, Y. Zhang, Y. Pan, X. Liu, G. Wang and D. Cao, *Electrochim. Acta*, 2014, **116**, 404–412.
- 50 C. Kim, P. J. Phillips, B. Key, T. Yi, D. Nordlund, Y. S. Yu, R. D. Bayliss, S. D. Han, M. He and Z. Zhang, *Adv. Mater.*, 2015, **27**, 3377–3384.
- 51 M. Cabello, R. Alcantara, F. Nacimiento, G. Ortiz, P. Lavela and J. Tirado, *CrystEngComm*, 2015, **17**, 8728–8735.
- 52 Z. Feng, X. Chen, L. Qiao, A. L. Lipson, T. T. Fister, L. Zeng, C. Kim, T. Yi, N. Sa and D. L. Proffit, *ACS Appl. Mater. Interfaces*, 2015, **7**, 28438–28443.
- 53 G. Liu, Q. Chi, Y. Zhang, Q. Chen, C. Zhang, K. Zhu and D. Cao, *Chem. Commun.*, 2018, **54**, 9474–9477.
- 54 S. Tao, W. Huang, Y. Liu, S. Chen, B. Qian and L. Song, *J. Mater. Chem.*, 2018, **6**, 8210–8214.
- 55 L. Hu, I. D. Johnson, S. Kim, G. M. Nolis, J. W. Freeland, H. D. Yoo, T. T. Fister, L. McCafferty, T. E. Ashton, J. A. Darr and J. Cabana, *Nanoscale*, 2019, **11**, 639–646.
- 56 M. Liu, A. Jain, Z. Rong, X. Qu, P. Canepa, R. Malik, G. Ceder and K. A. Persson, *Energy Environ. Sci.*, 2016, **9**, 3201–3209.
- 57 V. V. Kulish, D. Koch and S. Manzhos, *Phys. Chem. Chem. Phys.*, 2017, **19**, 6076–6081.
- 58 X. Sun, P. Bonnicks, V. Duffort, M. Liu, Z. Rong, K. A. Persson, G. Ceder and L. F. Nazar, *Energy Environ. Sci.*, 2016, **9**, 2273–2277.
- 59 P. Bonnicks, X. Sun, K.-C. Lau, C. Liao and L. F. Nazar, *J. Phys. Chem. Lett.*, 2017, **8**, 2253–2257.
- 60 A. James, J. B. Goodenough and N. Clayden, *J. Solid State Chem.*, 1988, **77**, 356–365.
- 61 V. Bodenez, L. Dupont, L. Laffont, A. Armstrong, K. Shaju, P. G. Bruce and J.-M. Tarascon, *J. Mater. Chem.*, 2007, **17**, 3238–3247.
- 62 R. Tressler, F. Hummel and V. Stubican, *J. Am. Ceram. Soc.*, 1968, **51**, 648–651.

- 63 Z. Jian, Y. S. Hu, X. Ji and W. Chen, *Adv. Mater.*, 2017, **29**, 1601925.
- 64 S. Chen, C. Wu, L. Shen, C. Zhu, Y. Huang, K. Xi, J. Maier and Y. Yu, *Adv. Mater.*, 2017, **29**, 1700431.
- 65 K. Makino, Y. Katayama, T. Miura and T. Kishi, *J. Power Sources*, 2001, **99**, 66–69.
- 66 K. Makino, Y. Katayama, T. Miura and T. Kishi, *J. Power Sources*, 2001, **97**, 512–514.
- 67 N. Anuar, S. Adnan and N. Mohamed, *Ceram. Int.*, 2014, **40**, 13719–13727.
- 68 Z.-D. Huang, T. Masese, Y. Orikasa and T. Mori, *RSC Adv.*, 2015, **5**, 8598–8603.
- 69 J. Zeng, Y. Yang, S. Lai, J. Huang, Y. Zhang, J. Wang and J. Zhao, *Chem. – Eur. J.*, 2017, **23**, 16898–16905.
- 70 J. Zeng, D. Wu, X. Wang, J. Wu, J. Li, J. Wang and J. Zhao, *Chem. Eng. J.*, 2019, **372**, 37–45.
- 71 N. Wu, Y.-C. Lyu, R.-J. Xiao, X. Yu, Y.-X. Yin, X.-Q. Yang, H. Li, L. Gu and Y.-G. Guo, *NPG Asia Mater.*, 2014, **6**, e120.
- 72 M. J. Aragón, P. Lavela, P. Recio, R. Alcántara and J. L. Tirado, *J. Electroanal. Chem.*, 2018, **827**, 128–136.
- 73 S. Redfern, G. Artioli, R. Rinaldi, C. Henderson, K. Knight and B. Wood, *Phys. Chem. Miner.*, 2000, **27**, 630–637.
- 74 Z. Feng, J. Yang, Y. NuLi, J. Wang, X. Wang and Z. Wang, *Electrochem. Commun.*, 2008, **10**, 1291–1294.
- 75 Z. Feng, J. Yang, Y. NuLi and J. Wang, *J. Power Sources*, 2008, **184**, 604–609.
- 76 Y. NuLi, J. Yang, J. Wang and Y. Li, *J. Phys. Chem. C*, 2009, **113**, 12594–12597.
- 77 Y. NuLi, J. Yang, Y. Li and J. Wang, *Chem. Commun.*, 2010, **46**, 3794–3796.
- 78 Y. Li, Y. Nuli, J. Yang, T. Yilinuer and J. Wang, *Chin. Sci. Bull.*, 2011, **56**, 386–390.
- 79 Y. NuLi, Y. Zheng, Y. Wang, J. Yang and J. Wang, *J. Mater. Chem.*, 2011, **21**, 12437–12443.
- 80 Y. NuLi, Y. Zheng, F. Wang, J. Yang, A. I. Minett, J. Wang and J. Chen, *Electrochem. Commun.*, 2011, **13**, 1143–1146.
- 81 Q. D. Truong, M. K. Devaraju and I. Honma, *J. Power Sources*, 2017, **361**, 195–202.
- 82 J. Heath, H. Chen and M. S. Islam, *J. Mater. Chem. A*, 2017, **5**, 13161–13167.
- 83 C. Ling, D. Banerjee, W. Song, M. Zhang and M. Matsui, *J. Mater. Chem.*, 2012, **22**, 13517–13523.
- 84 T. Mori, T. Masese, Y. Orikasa, Z.-D. Huang, T. Okado, J. Kim and Y. Uchimoto, *Phys. Chem. Chem. Phys.*, 2016, **18**, 13524–13529.
- 85 R. Zhang and C. Ling, *ACS Appl. Mater. Interfaces*, 2016, **8**, 18018–18026.
- 86 X. Chen, F. L. Bleken, O. M. Løvik and F. Vullum-Bruer, *J. Power Sources*, 2016, **321**, 76–86.
- 87 Y. Orikasa, T. Masese, Y. Koyama, T. Mori, M. Hattori, K. Yamamoto, T. Okado, Z.-D. Huang, T. Minato and C. Tassel, *Sci. Rep.*, 2014, **4**, 5622.
- 88 A. Torres and M. Arroyo-de Dompablo, *J. Phys. Chem. C*, 2018, **122**, 9356–9362.
- 89 A. Parija, D. Prendergast and S. Banerjee, *ACS Appl. Mater. Interfaces*, 2017, **9**, 23756–23765.
- 90 V. V. Kulish and S. Manzhos, *RSC Adv.*, 2017, **7**, 18643–18649.
- 91 A. Parija, Y. Liang, J. L. Andrews, L. R. De Jesus, D. Prendergast and S. Banerjee, *Chem. Mater.*, 2016, **28**, 5611–5620.
- 92 J. L. Andrews, A. Mukherjee, H. D. Yoo, A. Parija, P. M. Marley, S. Fakra, D. Prendergast, J. Cabana, R. F. Klie and S. Banerjee, *Chem*, 2018, **4**, 564–585.
- 93 J.-P. Monchoux, M. Dollé, P. Rozier and J. Galy, *Solid State Ionics*, 2011, **182**, 24–31.
- 94 T. Mueller, G. Hautier, A. Jain and G. Ceder, *Chem. Mater.*, 2011, **23**, 3854–3862.
- 95 J. Wu, G. Gao, G. Wu, B. Liu, H. Yang, X. Zhou and J. Wang, *RSC Adv.*, 2014, **4**, 15014–15017.
- 96 J. Wu, G. Gao, G. Wu, L. Liu, J. Ma and Y. Chen, *Phys. Chem. Chem. Phys.*, 2019, **21**, 4947–4952.
- 97 J. Wu, G. Gao, G. Wu, B. Liu, H. Yang, X. Zhou and J. Wang, *Phys. Chem. Chem. Phys.*, 2014, **16**, 22974–22978.
- 98 J. Wang, S. Tan, G. Zhang, Y. Jiang, Y. Yin, F. Xiong, Q. Li, D. Huang, Q. Zhang, L. Gu, Q. An and L. Mai, *Sci. China Mater.*, 2020, DOI: 10.1007/s40843-020-1311-1.
- 99 S.-H. Bo, C. P. Grey and P. G. Khalifah, *Chem. Mater.*, 2015, **27**, 4630–4639.
- 100 L. Zhou, F. Xiong, S. Tan, Q. An, Z. Wang, W. Yang, Z. Tao, Y. Yao, J. Chen and L. Mai, *Nano Energy*, 2018, **54**, 360–366.
- 101 S. Chakrabarti and K. Biswas, *J. Mater. Sci.*, 2017, **52**, 10972–10980.
- 102 B. Lee, E. Jo, J. Choi, J. H. Kim, W. Chang, S. Yu, H.-S. Kim and S. H. Oh, *J. Mater. Chem. A*, 2019, **7**, 25619–25627.
- 103 M. H. Han, E. Gonzalo, G. Singh and T. Rojo, *Energy Environ. Sci.*, 2015, **8**, 81–102.
- 104 Y. Zhang, G. Liu, C. Zhang, Q. Chi, T. Zhang, Y. Feng, K. Zhu, Y. Zhang, Q. Chen and D. Cao, *Chem. Eng. J.*, 2019, 123652.
- 105 R. D. Shannon, *Acta Crystallogr., Sect. A: Cryst. Phys., Diffraction, Theor. Gen. Crystallogr.*, 1976, **32**, 751–767.
- 106 M. Mao, X. Ji, S. Hou, T. Gao, F. Wang, L. Chen, X. Fan, J. Chen, J. Ma and C. Wang, *Chem. Mater.*, 2019, **31**, 3183–3191.
- 107 M. Levi, E. Lancri, E. Levi, H. Gizbar, Y. Gofer and D. Aurbach, *Solid State Ionics*, 2005, **176**, 1695–1699.
- 108 Y. Gu, Y. Katsura, T. Yoshino, H. Takagi and K. Taniguchi, *Sci. Rep.*, 2015, **5**, 12486.
- 109 D. Aurbach, G. S. Suresh, E. Levi, A. Mitelman, O. Mizrahi, O. Chusid and M. Brunelli, *Adv. Mater.*, 2007, **19**, 4260–4267.
- 110 Z. Wang, Y. Zhu, C. Qiao, S. Yang, J. Jia, S. Rafai, X. Ma, S. Wu, F. Ji and C. Cao, *Small*, 2019, **15**, 1902797.
- 111 J. T. Inconvati, L. F. Wan, B. Key, D. Zhou, C. Liao, L. Fuoco, M. Holland, H. Wang, D. Prendergast and K. R. Poepfelmeier, *Chem. Mater.*, 2015, **28**, 17–20.
- 112 L. F. Wan, J. T. Inconvati, K. R. Poepfelmeier and D. Prendergast, *Chem. Mater.*, 2016, **28**, 6900–6908.
- 113 X. Sun, P. Bonnick and L. F. Nazar, *ACS Energy Lett.*, 2016, **1**, 297–301.
- 114 B. Liu, T. Luo, G. Mu, X. Wang, D. Chen and G. Shen, *ACS Nano*, 2013, **7**, 8051–8058.

- 115 Z. Li, X. Mu, Z. Zhao-Karger, T. Diemant, R. J. Behm, C. Kübel and M. Fichtner, *Nat. Commun.*, 2018, **9**, 5115.
- 116 P. Jing, H. Lu, W. Yang and Y. Cao, *Electrochim. Acta*, 2020, **330**, 135263.
- 117 S. Tepavcevic, Y. Liu, D. Zhou, B. Lai, J. Maser, X. Zuo, H. Chan, P. Král, C. S. Johnson and V. Stamenkovic, *ACS Nano*, 2015, **9**, 8194–8205.
- 118 K. W. Nam, S. Kim, S. Lee, M. Salama, I. Shterenberg, Y. Gofer, J.-S. Kim, E. Yang, C. S. Park and J.-S. Kim, *Nano Lett.*, 2015, **15**, 4071–4079.
- 119 N. Sa, T. L. Kinnibrugh, H. Wang, G. Sai Gautam, K. W. Chapman, J. T. Vaughey, B. Key, T. T. Fister, J. W. Freeland and D. L. Proffitt, *Chem. Mater.*, 2016, **28**, 2962–2969.
- 120 X. Ji, J. Chen, F. Wang, W. Sun, Y. Ruan, L. Miao, J. Jiang and C. Wang, *Nano Lett.*, 2018, **18**, 6441–6448.
- 121 121E. A. Esparcia Jr, M. S. Chae, J. D. Ocon and S.-T. Hong, *Chem. Mater.*, 2018, **30**, 3690–3696.
- 122 X. Miao, Z. Chen, N. Wang, Y. Nuli, J. Wang, J. Yang and S.-I. Hirano, *Nano Energy*, 2017, **34**, 26–35.
- 123 H. D. Yoo, J. R. Jokisaari, Y.-S. Yu, B. J. Kwon, L. Hu, S. Kim, S.-D. Han, M. Lopez, S. H. Lapidus and G. M. Nolis, *ACS Energy Lett.*, 2019, **4**, 1528–1534.
- 124 M. Rastgoo-Deylami, M. S. Chae and S.-T. Hong, *Chem. Mater.*, 2018, **30**, 7464–7472.
- 125 G. Gershinsky, H. D. Yoo, Y. Gofer and D. Aurbach, *Langmuir*, 2013, **29**, 10964–10972.
- 126 X. Sun, V. Duffort, B. L. Mehdi, N. D. Browning and L. F. Nazar, *Chem. Mater.*, 2016, **28**, 534–542.
- 127 F. Liu, Y. Liu, X. Zhao, X. Liu and L.-Z. Fan, *J. Mater. Chem. A*, 2019, **7**, 16712–16719.
- 128 D.-M. Kim, S. C. Jung, S. Ha, Y. Kim, Y. Park, J. H. Ryu, Y.-K. Han and K. T. Lee, *Chem. Mater.*, 2018, **30**, 3199–3203.
- 129 L. Cui, L. Zhou, Y.-M. Kang and Q. An, *ChemSusChem*, 2020, **13**, 1071–1092.
- 130 G. S. Gautam, P. Canepa, R. Malik, M. Liu, K. Persson and G. Ceder, *Chem. Commun.*, 2015, **51**, 13619–13622.
- 131 J. Livage, *Chem. Mater.*, 1991, **3**, 578–593.
- 132 P. Novak and J. Desilvestro, *J. Electrochem. Soc.*, 1993, **140**, 140–144.
- 133 D. Imamura and M. Miyayama, *Solid State Ionics*, 2003, **161**, 173–180.
- 134 M. Vujković, I. Pašti, I. S. Simatović, B. Šljukić, M. Milenković and S. Mentus, *Electrochim. Acta*, 2015, **176**, 130–140.
- 135 D. Imamura, M. Miyayama, M. Hibino and T. Kudo, *J. Electrochem. Soc.*, 2003, **150**, A753–A758.
- 136 J.-N. Cha, B.-S. Cheong and H.-G. Cho, *J. Phys. Chem. A*, 2001, **105**, 1789–1796.
- 137 S. H. Lee, R. A. DiLeo, A. C. Marschilok, K. J. Takeuchi and E. S. Takeuchi, *ECS Electrochem. Lett.*, 2014, **3**, A87–A90.
- 138 Q. An, Y. Li, H. D. Yoo, S. Chen, Q. Ru, L. Mai and Y. Yao, *Nano Energy*, 2015, **18**, 265–272.
- 139 G. Sai Gautam, P. Canepa, W. D. Richards, R. Malik and G. Ceder, *Nano Lett.*, 2016, **16**, 2426–2431.
- 140 Y. Liang, H. D. Yoo, Y. Li, J. Shuai, H. A. Calderon, F. C. Robles Hernandez, L. C. Grabow and Y. Yao, *Nano Lett.*, 2015, **15**, 2194–2202.
- 141 S. D. Perera, R. B. Archer, C. A. Damin, R. Mendoza-Cruz and C. P. Rhodes, *J. Power Sources*, 2017, **343**, 580–591.
- 142 C. Wu, G. Zhao, S. Gong, N. Zhang and K. Sun, *J. Mater. Chem. A*, 2019, **7**, 4426–4430.
- 143 L. Zhou, Q. Liu, Z. Zhang, K. Zhang, F. Xiong, S. Tan, Q. An, Y. M. Kang, Z. Zhou and L. Mai, *Adv. Mater.*, 2018, **30**, 1801984.
- 144 H. D. Yoo, Y. Liang, H. Dong, J. Lin, H. Wang, Y. Liu, L. Ma, T. Wu, Y. Li and Q. Ru, *Nat. Commun.*, 2017, **8**, 339.
- 145 M. Xu, S. Lei, J. Qi, Q. Dou, L. Liu, Y. Lu, Q. Huang, S. Shi and X. Yan, *ACS Nano*, 2018, **12**, 3733–3740.
- 146 Y. Zhao, D. Wang, D. Yang, L. Wei, B. Liu, X. Wang, G. Chen and Y. Wei, *Energy Storage Mater.*, 2019, **23**, 749–756.
- 147 Y. Li, Y. Lu, P. Adelhelm, M.-M. Titirici and Y.-S. Hu, *Chem. Soc. Rev.*, 2019, **48**, 4655–4687.
- 148 Y. Liu, B. V. Merinov and W. A. Goddard, *Proc. Natl. Acad. Sci. U. S. A.*, 2016, **113**, 3735–3739.
- 149 D. S. Tchitchekova, A. Ponrouch, R. Verrelli, T. Broux, C. Frontera, A. Sorrentino, F. Bardé, N. Biskup, M. E. Arroyo-de Dompablo and M. R. Palacín, *Chem. Mater.*, 2018, **30**, 847–856.
- 150 Y. Zhao, C. Han, J. Yang, J. Su, X. Xu, S. Li, L. Xu, R. Fang, H. Jiang and X. Zou, *Nano Lett.*, 2015, **15**, 2180–2185.
- 151 H. Tang, F. Xiong, Y. Jiang, C. Pei, S. Tan, W. Yang, M. Li, Q. An and L. Mai, *Nano Energy*, 2019, **58**, 347–354.
- 152 X. Yao, Y. Zhao, F. A. Castro and L. Mai, *ACS Energy Lett.*, 2019, **4**, 771–778.
- 153 Y. Xu, X. Deng, Q. Li, G. Zhang, F. Xiong, S. Tan, Q. Wei, J. Lu, J. Li and Q. An, *Chem*, 2019, **5**, 1194–1209.
- 154 X. Deng, Y. Xu, Q. An, F. Xiong, S. Tan, L. Wu and L. Mai, *J. Mater. Chem. A*, 2019, **7**, 10644–10650.
- 155 T. Koketsu, J. Ma, B. J. Morgan, M. Body, C. Legein, W. Dachraoui, M. Giannini, A. Demortière, M. Salanne and F. Dardoize, *Nat. Mater.*, 2017, **16**, 1142.
- 156 Y. Wang, X. Xue, P. Liu, C. Wang, X. Yi, Y. Hu, L. Ma, G. Zhu, R. Chen and T. Chen, *ACS Nano*, 2018, **12**, 12492–12502.
- 157 T. S. Arthur, K. Kato, J. Germain, J. Guo, P.-A. Glans, Y.-S. Liu, D. Holmes, X. Fan and F. Mizuno, *Chem. Commun.*, 2015, **51**, 15657–15660.
- 158 V. Mathew, S. Kim, J. Kang, J. Gim, J. Song, J. P. Baboo, W. Park, D. Ahn, J. Han and L. Gu, *NPG Asia Mater.*, 2014, **6**, e138.
- 159 Z. Wei, D. Wang, X. Yang, C. Wang, G. Chen and F. Du, *Adv. Mater. Interfaces*, 2018, **5**, 1800639.
- 160 Y. Cheng, Y. Shao, V. Raju, X. Ji, B. L. Mehdi, K. S. Han, M. H. Engelhard, G. Li, N. D. Browning and K. T. Mueller, *Adv. Funct. Mater.*, 2016, **26**, 3446–3453.
- 161 Q. D. Truong, M. Kempaiah Devaraju, D. N. Nguyen, Y. Gambe, K. Nayuki, Y. Sasaki, P. D. Tran and I. Honma, *Nano Lett.*, 2016, **16**, 5829–5835.
- 162 J. Köhler, N. Imanaka and G.-Y. Adachi, *Chem. Mater.*, 1998, **10**, 3790–3812.
- 163 R. Kitaura, F. Iwahori, R. Matsuda, S. Kitagawa, Y. Kubota, M. Takata and T. C. Kobayashi, *Inorg. Chem.*, 2004, **43**, 6522–6524.

- 164 W. Kaveevivitchai and A. J. Jacobson, *Chem. Mater.*, 2013, **25**, 2708–2715.
- 165 W. Kaveevivitchai and A. J. Jacobson, *Chem. Mater.*, 2016, **28**, 4593–4601.
- 166 A. Emly and A. Van der Ven, *Inorg. Chem.*, 2015, **54**, 4394–4402.
- 167 J. Qian, C. Wu, Y. Cao, Z. Ma, Y. Huang, X. Ai and H. Yang, *Adv. Energy Mater.*, 2018, **8**, 17026191.
- 168 K. Hurlbutt, S. Wheeler, I. Capone and M. Pasta, *Joule*, 2018, **2**, 1950–1960.
- 169 S. Yagi, M. Fukuda, T. Ichitsubo, K. Nitta, M. Mizumaki and E. Matsubara, *J. Electrochem. Soc.*, 2015, **162**, A2356–A2361.
- 170 Y. Mizuno, M. Okubo, E. Hosono, T. Kudo, K. Oh-ishi, A. Okazawa, N. Kojima, R. Kuroono, S.-I. Nishimura and A. Yamada, *J. Mater. Chem.*, 2013, **1**, 13055–13059.
- 171 Y. Mizuno, M. Okubo, E. Hosono, T. Kudo, H. Zhou and K. Oh-ishi, *J. Phys. Chem. C*, 2013, **117**, 10877–10882.
- 172 R. Y. Wang, C. D. Wessells, R. A. Huggins and Y. Cui, *Nano Lett.*, 2013, **13**, 5748–5752.
- 173 A. L. Lipson, S.-D. Han, S. Kim, B. Pan, N. Sa, C. Liao, T. T. Fister, A. K. Burrell, J. T. Vaughey and B. J. Ingram, *J. Power Sources*, 2016, **325**, 646–652.
- 174 L. Chen, J. L. Bao, X. Dong, D. G. Truhlar, Y. Wang, C. Wang and Y. Xia, *ACS Energy Lett.*, 2017, **2**, 1115–1121.
- 175 X. Sun, V. Duffort and L. F. Nazar, *Adv. Sci.*, 2016, **3**, 1600044.
- 176 M. S. Chae, J. Hyoung, M. Jang, H. Lee and S.-T. Hong, *J. Power Sources*, 2017, **363**, 269–276.
- 177 P. Marzak, M. Kosiahn, J. Yun and A. S. Bandarenka, *Electrochim. Acta*, 2019, **307**, 157–163.
- 178 Y. Wang, Z. Liu, C. Wang, X. Yi, R. Chen, L. Ma, Y. Hu, G. Zhu, T. Chen and Z. Tie, *Adv. Mater.*, 2018, **30**, 1802563.
- 179 C. Pei, Y. Yin, R. Sun, F. Xiong, X. Liao, H. Tang, S. Tan, Y. Zhao, Q. An and L. Mai, *ACS Appl. Mater. Interfaces*, 2019, **11**, 31954–31961.
- 180 Y. Wang, C. Wang, X. Yi, Y. Hu, L. Wang, L. Ma, G. Zhu, T. Chen and Z. Jin, *Energy Storage Mater.*, 2019, **23**, 741–748.
- 181 Z. Li, S. Ding, J. Yin, M. Zhang, C. Sun and A. Meng, *J. Power Sources*, 2020, **451**, 227815.
- 182 P. Jing, H. Lu, W. Yang, Y. Cao, B. Xu, W. Cai and Y. Deng, *Ionics*, 2020, **26**, 777–787.
- 183 K. Taniguchi, Y. Gu, Y. Katsura, T. Yoshino and H. Takagi, *Appl. Phys. Express*, 2015, **9**, 11801.
- 184 W. Yuan and J. R. Günter, *Solid State Ionics*, 1995, **76**, 253–258.
- 185 R. Sun, Q. Wei, Q. Li, W. Luo, Q. An, J. Sheng, D. Wang, W. Chen and L. Mai, *ACS Appl. Mater. Interfaces*, 2015, **7**, 20902–20908.